Laser Powder Bed Fusion of β-21S Titanium Alloy

Maria Macias-Sifuentes

Department of Mining and Materials Engineering
McGill University, Montreal, Quebec

November 2021

A thesis submitted to McGill University in partial fulfillment of the requirements of the degree of Master of Engineering

Abstract

Laser powder bed fusion (LPBF), one of the most studied processes among metal additive manufacturing (AM), has raised attention due to its high degree of manufacturing freedom, its ability to produce lightweight intricate components, and its energy-efficient, and time saving route. Today, research has focused only on a limited number of alloys such as Ti-6Al-4V, Inconel 625 and 718, and stainless steel 316L. New alloys produced by this technique need to be studied to be able to maximize the advantages of AM.

Metastable β-titanium alloys are attractive for the aerospace industry due to their low density, high strength, excellent hardenability, and stability at high temperature. Among these alloys, β-21S is known to offer improved elevated temperature strength, creep resistance, thermal stability, and oxidation resistance. Furthermore, heat treatment can be applied to this alloy for tailoring the mechanical properties according to the desired application.

The manufacturability of β-21S produced by LPBF, as well as the effect of heat treatment was investigated in the present thesis, to understand the relationship between the microstructure and the mechanical properties.

The tensile performance of β-21S in the as-built state presented comparable behavior to the wrought in solution treatment condition. Solution treatment and aging (STA) of the alloy precipitated the α-phase, increasing the microhardness, and strength, while reducing the ductility. The heat treatment applied to LPBF β-21S had a similar effect compared to β-21S fabricated by non-AM techniques. The properties obtained demonstrated the potential of β-21S for LPBF applications.

Résumé

La fusion laser sur lit de poudre ou laser powder bed fusion (LPBF), l'un des processus les plus étudiés parmi la fabrication additive métallique (FAM), a attiré l'attention en raison de son degré élevé de liberté de fabrication, de sa capacité à produire des composants complexes légers, de son efficacité énergétique et de son temps itinéraire de sauvegarde. Aujourd'hui, les recherches ne portent que sur un nombre limité d'alliages tels que le Ti-6Al-4V, l'Inconel 625 et 718, et l'acier inoxydable 316L. De nouveaux alliages produits par cette technique doivent être étudiés pour pouvoir maximiser les avantages de la FAM. Les alliages de β-titane métastables sont attrayants pour l'industrie aérospatiale en raison de leur faible densité, de leur haute résistance, de leur excellente trempabilité et de leur stabilité à haute température. Parmi ces alliages, le β-21S est connu pour offrir une résistance aux températures élevées, une résistance au fluage, une stabilité thermique et une résistance à l'oxydation améliorées. De plus, un traitement thermique peut être appliqué à cet alliage pour adapter les propriétés mécaniques en fonction de l'application souhaitée. La fabricabilité du β-21S produit par LPBF, ainsi que l'effet du traitement thermique ont été étudiés dans la présente mémoire, pour comprendre la relation entre la microstructure et les propriétés mécaniques. Les performances de traction du β-21S à l'état tel que construit ont présenté un comportement comparable à celui du traitement forgé en solution. Le traitement en solution et le vieillissement de l'alliage ont précipité la phase, augmentant la micro-dureté et la résistance, tout en réduisant la ductilité. Le traitement thermique appliqué au LPBF β-21S a eu un effet similaire à celui du β-21S fabriqué par des techniques non AM. Les propriétés obtenues ont démontré le potentiel du β-21S pour les applications LPBF.

Acknowledgements

Undertaking a master's degree at McGill has been an eventful and challenging journey. I would like to express my deepest appreciation to Prof. Mathieu Brochu for his excellent guidance and supervision. He provided a great source of knowledge, opportunities, and resources for my development during this journey.

I would also like to extend my deepest gratitude to the researchers I worked closely with: Oscar, Sila, Alberto, Sun Yong, Pierre, Ivonne and Xianglong. They provided great support and guidance at every step of this project.

Special thanks to every person I came across while working at the Powder Processing and Additive Manufacturing (P^2AM^2) group. It has been a pleasure to be part of such a big family.

I gratefully acknowledge the assistance of Barbara, Dr. Florence, and all the other staff and professors from the Mining and Materials department. For all their hard work to keep the department running, especially during the hard time of the pandemic.

I am very grateful for the generous research support I received from the Natural Sciences and Engineering Research Council of Canada (NSERC, Project Number: CRDPJ 517633–17). Likewise, special thanks to the Consejo Nacional de Ciencia y Tecnología (CONACYT, Mexico) for their funding.

I would also like to extend my gratitude to all the people who helped me with their presence and support during this journey. Salvador, who had an important role in the development of my project since the beginning of it. Alejandra, a great friend I made in McGill and who was always there for me. Special thanks to my family and friends in Mexico, who provided their unconditional love and support during these hard times of pandemic. And finally, I very much appreciate friends I made in Montreal, special thanks to Daniel, Paulina and Oscar, who made the pandemic times so much more enjoyable. Without them it could not have been possible.

Contents

Abstract I
Résumé II
Acknowledgements III
List of Figures VI
List of Tables IX
Chapter 1 – Introduction and motivation 1
1.1 Additive Manufacturing and Laser powder bed fusion 1
1.1.1 Benefits and challenges of additive manufacturing 2
1.2 Objectives 3
Chapter 2 – Literature Review 5
2.1 Titanium alloys and metastable β-titanium alloys 5
2.1.1 Titanium β-21S 8
2.2 Heat treatment of metastable β-titanium alloys 8
2.2.1 Mechanical properties of heat treated β-21S 11
2.3 Heat treatment of laser powder bed fusion metastable β-titanium alloys 12
2.4 Laser powder bed fusion of metastable β-titanium alloys 14
2.5 Fracture surface of metastable β-titanium alloys 19
Chapter 3 – Experimental Methodology 23
3.1 Powder Characterization 23
3.1.1 Particle size distribution 23
3.1.2 Surface Morphology 24
3.1.3 Flowability 24
3.2 LPBF manufacturing 25
3.3 Metallurgical Characterization Techniques 26
3.3.1 Metallographic Specimen preparation 26
3.3.2 Optical Microscopy 26
3.3.3 Analysis software 27
3.3.4 Experimental density 27
3.3.5 X-Ray Diffraction 28
3.3.6 Scanning Electron Microscopy 29
3.3.7 Backscattering Electron Microscopy 29

3.3.8 Energy Dispersive Spectroscopy 29
3.3.9 Post processing heat treatment 30
3.3.10 Mechanical properties 30
Chapter 4 – Microstructure and mechanical properties of β-21S Ti alloy fabricated through laser powder bed fusion 31
4.1 Preface 31
4.2 Abstract 31
4.3 Introduction. 32
4.4 Materials and methods. 33
4.5 Results. 36
4.6 Conclusions 47
Chapter 6 – Conclusion and summary 53
Chapter 7 References 54

List of Figures

Figure 1 Representative steps of AM LPBF (adapted and modified from Calignano et. al [3]) 1

Figure 2 a) Generic illustration of LPBF (adapted from Kurzynowski et al. [5]) b) Common process parameters in laser powder bed fusion AM (adapted from Oliveira et al. [4]) 2

Figure 3 Unit cell of α-phase (adapted from Lütjering and Williams [19]) 5

Figure 4 Unit cell of β-phase (adapted from Lütjering and Williams [19]) 5

Figure 5 Pseudo-binary section through a β isomorphous phase diagram (schematically) (adapted from Lütjering and Williams [19]) 6

Figure 6 A schematic illustration of a) super-transus solution treatment in the β field and, b) sub-transus solution treatment in the α-β field, both followed by isothermal aging (adopted from Kolli and Devaraj [19]) 9

Figure 7 Ti-3.5Al-5Mo-4V microstructure after solution treatment and double aged for 2 h at 300 °C and 500 °C for 8 h (adapted from Ji et al. [31]) 10

Figure 8 β-21S microstructure after solution treatment at 900 °C for 30 min and water quench (WQ), followed by aging a) 400 °C for 5 h, WQ and 600 °C for 1 h, WQ; and b) 690 °C for 8 h, furnace cooled (FC) and 640 °C for 8 h, FC presenting α-phase on a β-matrix and PFZ (adapted from Mantri et al. [27]) 10

Figure 9. β-21S microstructures presenting recrystallized β-grains after different solution treatments: a) at 870 °C (adapted from Xu et al. [35]) and, c) at 845 °C (adapted from Agarwal et al. [26]) 11

Figure 10 β-21S microstructure after solution treatment 30 min at 845 °C followed by aging 8 h at ~540 °C: a) adapted from Agarwal et al. [26], b) adapted from Huang et al. [36] 12

Figure 11 Different metastable AM β-alloys after STA: a-b) Ti–3Al–8V–6Cr–4Mo–4Z (adapted from Bermingham et al. [39]) c-d) Ti-5Al-5Mo-5V-3Cr-1Zr (adapted from Deng et al. [38]) e-f) Ti-6Nb-5Al-5Mo-3Cr-0.5Fe (adapted from Da Costa et al [39]) 13

Figure 12 Molten pool shape presented for metastable β-titanium alloys a) Ti-Cr (adapted from Nagase et al. [44]), b) β-21S (adapted from Pellizari [45]), c) Ti-15Mo-5Zr-3Al (adapted from Nakano et al. [41]) 15

Figure 13 SEM images presenting the parallel orientation on the surface dendrites respect to the <100> crystallographic direction on LPBF Ti–5Al–5V–5Mo–3Cr–0.5 Fe (adapted from Zafari et al. [46]) 16

Figure 14 EBSD phase maps and pole figures of AM metastable β-titanium alloys: a)-b) Ti–26Nb (adapted from Fischer et al. [48]), c)-d) Ti-12Mo-6Zr-2Fe (adapted from Duan et al. [49]) 17

Figure 15 XRD of SLM Ti-6Al-4V Eli +10Mo as built and after different heat treatments (adapted from Vrancken et al. [50]) 18

Figure 16 Microstructures observed in AM metastable β-titanium alloys: a) Ti-5Al-5V-5Mo-3Cr (adapted from Zafari et al. [46]) b) Ti–26Nb (adapted from Fischer [48]) 18

Figure 17 LPBF β-21S a) SEM micrograph presenting columnar β grains along the building direction b) pole figures presented (adapted from Pellizari et al. [45]) 19

Figure 18 a-b) AB Ti-5Al-5Mo-5V-3Cr-1Zr presenting ductile fracture (adapted from Deng et al. [38]); c-d) AB Ti-10V-2Fe-3Al presenting ductile fracture of β-elongated grains (adapted from Qui et al. [51]) 20

Figure 19 Ti-10V-2Fe-3Al a) EBSD b) intergranular fracture of β-equiaxed grains c) localized plasticity of the β-equiaxed grains 20

Figure 20 SLM Ti-5Al-5Mo-5 V-3Cr-1Zr a) microstructure b) fracture surface presenting intragranular fracture (adapted from Deng et al. [38]) 22

Figure 21 Wrought β-21S presenting different a-d) microstructures and c-h) their respetive surface fracture (adapted from Mantri et al. [27]) 22

Figure 22 Particle size distribution of Ti β-21S 24

Figure 23 GranuDrum apparatus 25

Figure 24 Cohesive index of Ti β-21S 25

Figure 25 Renishaw AM 400 26

Figure 26 Schematic illustrations of the plane used for microstructural analyses for Chapter 4 . 26

Figure 27 Nikon light optical microscope 27

Figure 28 Bruker D8 Discovery XRD 28

Figure 29 Hitachi 3500 SEM 29

Figure 30 Schematic of the heat treatment tested in this study 30

Figure 31 SEM micrographs showing the size, shape and morphology of the β-21S particles ... 34

Figure 32 (a) Particle size distribution and (b) cohesive index of Ti β-21S 34

Figure 33 Schematic of the heat treatment tested in this study 35

Figure 34 (a) Schematic illustrations of the plane used for microstructural analysis (b) Optical image showing the relative density in AB condition 36

Figure 35 (a) XRD, (b) phase map of the AB sample 37

Figure 36 The calculated CCT and TTT diagrams for β-21S. Blue line: TTT diagram, red line CCT diagram for α-phase with volume fraction of 10^{-4}. Dashed lines indicate the cooling rates 10^{4} °C/s and 10^{3} °C/s 38

Figure 37 Images showing the microstructure after etching in AB condition at different magnifications (a) OM, (b) SEM 39

Figure 38 EBSD analysis of the AB sample 40

Figure 39 XRD pattern STA condition 40

Figure 40 SEM micrographs showing the microstructure after etching of samples STA at different magnifications 42

Figure 41 EDS line scan of the STA alloy 43

Figure 42 (a) YS, (b) UTS as a function of elongation at RT. Grey cube and red diamond denoted with green lines represent the values of β-21S in the present study: AB, and STA, respectively. Black triangles pointing up, and blue triangles pointing down represent wrought samples in: ST, and STA, respectively 44

Figure 43 SEM micrograph of fracture surface. AB condition 45

Figure 44 SEM micrographs of fracture surface at different magnification. STA condition 46

Figure 45 (a) YS, (b) UTS as a function of elongation at 450 °C. Red diamonds represent the values of β-21S STA in the present study. Triangles represent wrought samples in STA condition 47

Figure 46 SEM micrographs of fracture surface at 450°C, STA condition 47

List of Tables

Table 1 Mechanical properties at room temperature of β-21S after ST (845-850 °C) 11
Table 2 Mechanical properties of β-21S after STA (ST 845-850 °C and A 540 °C) 12
Table 3 Mechanical properties of different β-titanium alloys produced by AM and heat treated 14
Table 4 Chemical composition of β-21S powder from the certificate of conformity of the supplier. 23
Table 5 Chemical composition of β-21S powder from the certificate of conformity of the supplier. 33

Chapter 1 – Introduction and motivation

1.1 Additive Manufacturing and Laser powder bed fusion

Additive manufacturing (AM) is a fabrication process to make objects from 3D model data, by joining layer upon layer, without the need of part-depending tools such as in subtractive manufacturing methodologies [1,2]. To supplement the established subtractive manufacturing process (milling or turning), formative manufacturing, (casting or forging [2]), AM is becoming the third important pillar of the manufacturing technologies.

Laser powder bed fusion (LPBF) is a popular AM technique allowing quick production of 3D parts with complicated shapes directly from powders. The LPBF process workflow can be divided into three important steps: design, process, and post-processing as represented in Figure 1.

First, as part of the design stage, the model generation through a 3D CAD data set is created. This 3D CAD is then converted into a STL file to be used during the print.

In the second step, the structure is sliced and then used as base point to create the physical part over a base plate, typically of the same material. Each slice will be used to spread a layer of powder that will be part of the final component. Each layer is bonded to the preceding layer by an energy source (e.g. laser beam in the case of LPBF). Layer by layer, the physical model is growing from the bottom to the top until the final part is obtained.

The third step consists of the part removal and final finishing of the part, if needed.

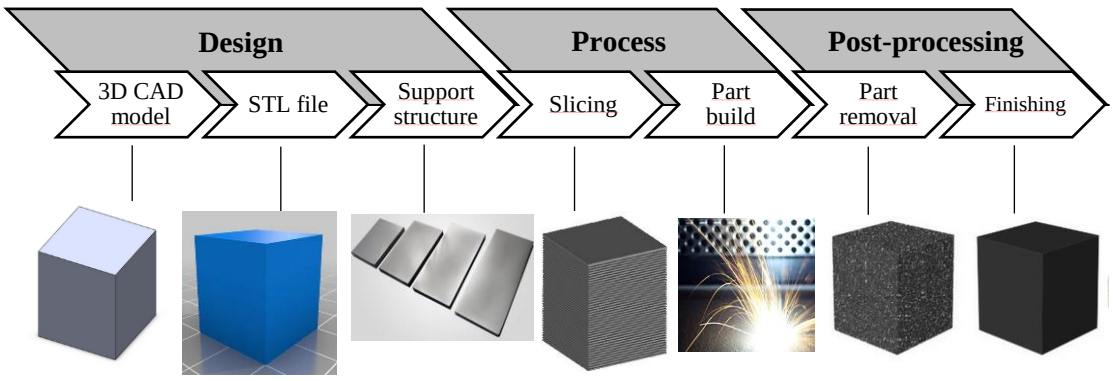

Figure 1 Representative steps of AM LPBF (adapted and modified from Calignano et. al [3])

Figure 2 a) presents a generic illustration of the LPBF system consisting of a laser beam, scanning mirrors, the powder bed and the powder spreader. Since the LPBF is a very complex process, manufacturers of metal AM systems provide a set of processing parameters according to the material to be printed. From this set of parameters, investigations are performed regarding the modification and optimization according to the desired characteristics of the final part. The parameters commonly considered to be modified include laser power, layer thickness, laser scan velocity, distance between laser passes (also known as hatch distance) and scanning strategies (laser scanning pattern on each layer). Figure 2 b) presents these parameters [4].

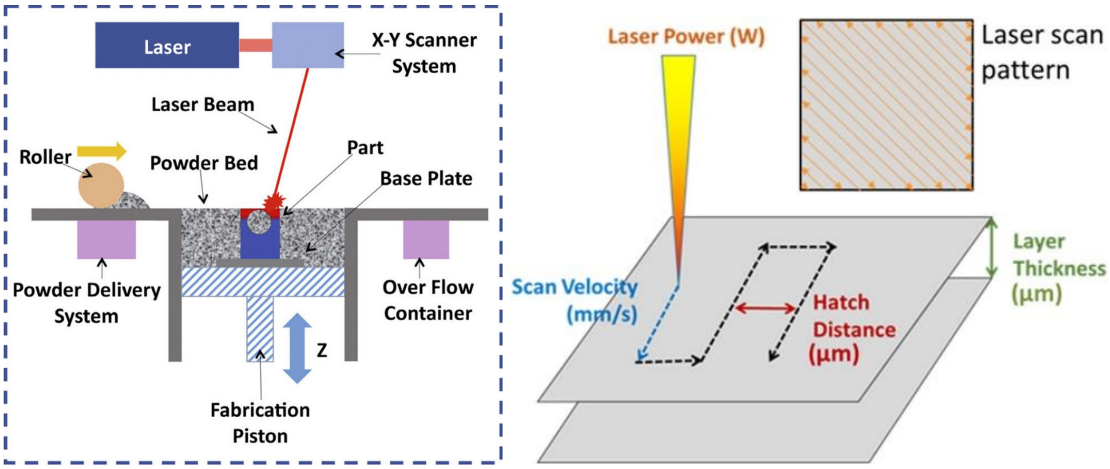

Figure 2 a) Generic illustration of LPBF (adapted from Kurzynowski et al. [5]) b) Common process parameters in laser powder bed fusion AM (adapted from Oliveira et al. [4])

1.1.1 Benefits and challenges of additive manufacturing

The speed advantage of AM is not only in terms of the time required to build parts but also on the whole product development process. On one hand, the product development process is being simplified since 3D CAD is used as starting point. Using 3D CAD provides preview of the design intent, and no conversion needs to be done. Moreover, the simplification of the process can be seen in terms of the reduction in process steps.

Another benefit comes from the resources required to produce a part, such as skilled personnel. Furthermore, workshops which adopt AM technology can be much cleaner, more streamlined, and versatile than before [6].

Since AM of metals is a relatively new technology, there are still many challenges related to its use. These challenges can be technical or associated with the material to be manufactured, i.e., metallurgical.

AM involves directional heat extraction, repeated melting and rapid solidification that complicate the thermal history of the produced alloy. In addition, repeated solid-state phase transformations can also be produced in some AM alloys. These factors are not typically found in conventional processes and introduce some complexities such as heterogeneous microstructures and anisotropic mechanical properties [7,8]. Therefore, more research is needed to open the potential for more alloys to be manufactured by AM. Today, research was mainly focused only on a limited number of alloys, for example Ti-6Al-4V [9,10], nickel Inconel 625 and 718 [11,12], and stainless steels [13,14]. New alloys produced by this technique need to be studied to be able to maximize the advantages of AM.

Metastable β titanium alloys are attractive for AM due to their excellent characteristics that include excellent mechanical properties, low density, and good corrosion resistance; as well as the high costs involved in the production of these alloys. In this context, AM can lead to significant saving in machining and fabricating costs [1,15,16]. These advantages might specially benefit the aerospace sector, due to the difficulty of machining high performance alloys such as titanium and given that as little as 5% of the raw material may remain in the finished parts when fabricated by conventional methods [17].

Today, AM techniques face certain challenges achieving quality consistency, especially in producing fully dense metal parts. To be able to compete against traditional methods, LPBF requires inclusion of new alloys with optimized material response, fabricating dense materials and controlling the mechanical performance.

1.2 Objectives

In the current context, a knowledge gap in the LPBF of Ti β-S21 exist, and fulfilling this gap is the main objective of this thesis. The following sub-objectives of the present study are:

- Evaluate the LPBF manufacturability of a metastable β-titanium alloy, β-21S.

- Evaluate the response of the LPBF parts to conventional heat treatment, targeting application in the aerospace industry. In both states, microstructural characterization and evaluation of mechanical properties was used as a metric for comparison.

Chapter 2 – Literature Review

2.1 Titanium alloys and metastable β-titanium alloys

Titanium alloys have a wide range of mechanical and physical properties. These properties are primarily driven by its allotropy in the solid state. There are two main crystallographic allotropes existing in titanium alloys, which are the hexagonal close-packed (HCP) α-phase with its crystal structure displayed in Figure 3 and the higher-temperature body-centered cubic (BCC) β-phase with its crystal structure displayed in Figure 4 [18,19].

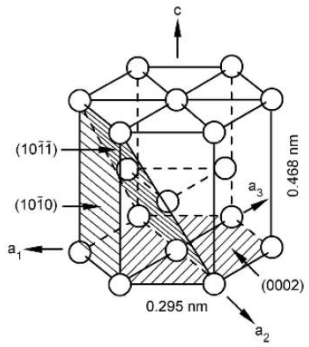

Figure 3 Unit cell of α-phase (adapted from Lütjering and Williams [19])

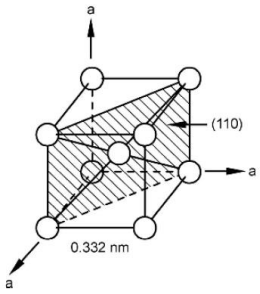

Figure 4 Unit cell of β-phase (adapted from Lütjering and Williams [19])

Titanium alloys contain different alloying elements that are usually classified into α- or β-stabilizer, depending on whether they increase or decrease the α/β transformation temperature of 882 °C reported for pure titanium [19]. Titanium alloys are classified into four different families: α, α+β, metastable β and β alloys [18,19], according to the concentration of β-stabilizing elements present in the respective composition. Figure 5 presents a pseudo-binary section through a β-isomorphous phase diagram showing the four classification of titanium alloys. The β-stabilizing elements concentration can be calculated by using Equation 1 as will be described below.

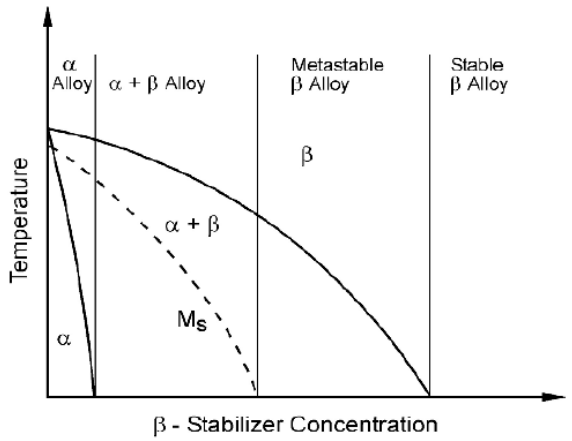

Figure 5 Pseudo-binary section through a β isomorphous phase diagram (schematically) (adapted from Lütjering and Williams [19])

The α-phase titanium alloys contain mainly α-phase with a small amount of β phase. They have relatively low strength, good corrosion resistance and are used in non-structural applications [19]. The elements commonly present on these alloys are Al, O, N, and C to stabilize the α-phase [18,19]. The α-phase titanium alloys have important strength limitations since solution strengthening by interstitials leads to strain localization and solid solution additions reduce the formability of the material [19].

α + β titanium alloys are containing both HCP and BCC phases with morphology and volume fraction depending on the composition of the alloy and imposed thermo-mechanical processing schedule. These alloys have relatively high strength, good toughness, good fatigue behavior, and excellent corrosion resistance [19]. These alloys often contain Al as α-phase stabilizing element and contain V or Mo as β-phase stabilizing elements. Solution treatment and age hardening are often used to control the final microstructure [18].

Metastable β-phase alloys contain mainly the β phase. As α + β titanium alloys, these alloys often contain Al as α-phase stabilizing, but include a higher percentage of β stabilizing elements such as Mo, V and Nb [20]. These alloys are especially attractive for their physical behavior advantages, and low density [18,21]. These characteristics make them an attractive choice for advanced engineering applications such as aircraft structures despite their high costs [18]. For example, Beta C, is used in aircraft springs and fasteners [18] and Ti-13V-l1Cr-3Al (wt. %) is used for application in the structure and landing gear of the SR-71 “BlackBird” aircraft [18].

Metastable β-phase alloys offer high specific strength, high ductility, low elastic modulus, good fatigue resistance, sufficient toughness, excellent corrosion resistance, and good formability, which makes them attractive for structural applications [21,22]. These properties are normally obtained after heat treatment.

To delineate the families based on alloying element content, the molybdenum equivalency (MoE) equation has been formulated to describe the stabilization of the β-phase. The MoE includes the different elements normally used in titanium alloys and normalize their β-phase stabilization.

There are different versions with minor variations of this equation (Bania [20], Cotton et al. [23], and Welsch et al. [24]), but the most commonly used is given in (1):

$$\begin{aligned} \text{MoE} = & 1.0\,(\text{wt. \% Mo}) + 0.67\,(\text{wt. \% V}) + 0.44(\text{wt. \% W}) + 0.28(\text{wt. \% Nb}) + 0.22(\text{wt. \% Ta}) + 2.9\,(\text{wt. \% Fe}) + 1.6\,(\text{wt. \% Cr}) + 1.25\,(\text{wt. \% Ni}) + \\ & 1.70(\text{wt. \% Mn}) + 1.70(\text{wt. \% Co}) - 1.0(\text{wt. \% Al}) \end{aligned} \quad (1)$$

This equation was calculating by experimental knowledge. It arbitrarily uses molybdenum as a baseline. The constant before each alloying element reflects the ratio of the β_c (approximate wt. % needed to retain 100% beta upon quenching) for the molybdenum baseline (Ie., 10.0) divided by the β_c for the specific element. Aluminum is added as a negative value to reflect its opposite tendency to stabilize alpha [20].

This equation can be used to further sub-divide metastable β alloys. Alloys with $0 \leq \text{MoE} < 5$ are β-rich, alloys with $5 \leq \text{MoE} < 10$ are near-β, alloys with $10 \leq \text{MoE} < 30$ are metastable-β, and alloys with $\text{MoE} > 30$ are known as stable-β [18]. In general, a MoE value of 10.0 is required to stabilize the BCC β-phase during quenching from above the β-transus temperature. The β-transus temperature is the boundary between the single-phase beta region and the two phase alpha-beta region, it generally decreases with increasing MoE value [18]. In the case of metastable β-titanium alloys, the β-transus is typically around 800 °C.

Metastable β-phase alloys consist predominantly of the BCC β-phase but can also contain small volume fractions of other phases such as α or ω-phase, depending on composition and thermo-mechanical processing [25,18].

2.1.1 Titanium β-21S

Among the metastable β-phase alloys, β-21S with a nominal weight percent composition of 15Mo, 3Al, 3Nb and 0.2Si, possesses all the previously mentioned benefits. Interestingly, β-21S can retain its strength at higher temperatures and display superior oxidation resistance than most β-alloys [26-28].

β-21S is commonly used in aerospace applications for warm to hot structures including ducts, engines plug, and nozzles. In fact, the main aerospace application is on the Boeing 777 exhaust nozzle [26,27], while Pratt and Whitney have selected it for some of its engines [26] due to the excellent mechanical property retention at high temperatures. The normal operating temperatures ranges of this alloy goes from 480-565 °C [26], with outstanding performance up to 650 °C (for short durations) [27].

In addition, β-21S has excellent resistance to high temperature hydraulic fluid (corrosion), which makes this alloy attractive for aircraft applications. The hydraulic fluid in commercial aircraft produces organo-phosphoric acid at around 130 °C that progressively corrodes and reduces thickness of parts. This corrosion also generates hydrogen that is absorbed and eventually leads to hydrogen embrittlement. The presence of Nb and Mo in β-21S make it more resistant to such attack. This has facilitated its use for nacelle applications at temperatures higher than 130 °C, replacing heavier steels and nickel base superalloys resulting in considerable weight saving [26].

β-21S has a MoE value of 12.84, calculated using Equation

(1**)**, which confirms the β-phase will be found at room temperature. It may also contain other phases depending on the thermo processing encountered by the alloy. The relatively high MoE reduced the T_β, which was reported to be 805 °C [29].

2.2 Heat treatment of metastable β-titanium alloys

Typically, the heat treatment applied to metastable β-titanium alloys are composed of a solution treatment followed by aging.

The solution treatment can be done below or above the β-transus temperature, as presented schematically on Figure 6. These two temperature schedules are normally categorized as β-solution treatment and α-β solution treatment, respectively [18]. The selected solution treatment for this project was β-solution treatment and is further referred to as ST hereafter.

ST is performed to homogenize the microstructure, developing the β-phase and resulting in low strength and high ductility [18,30]. However, ST for extended period of time can result in excessive grain growth and coarsening that will negatively affect the mechanical properties [18]. In that context, ST is done slightly above 805 °C for a relatively short period of time [30].

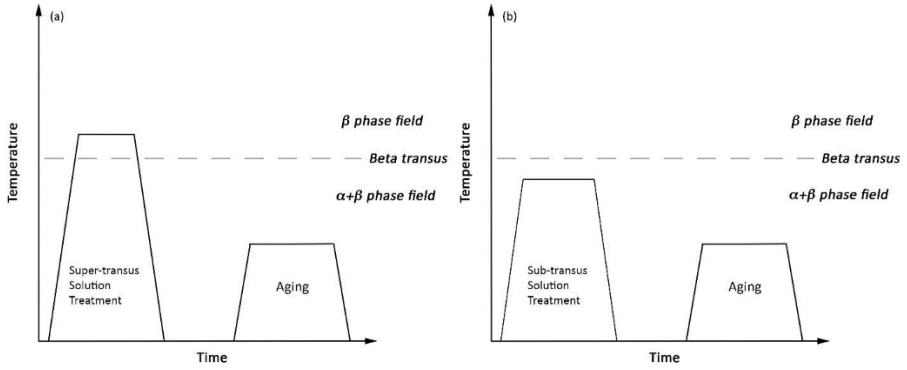

Figure 6 A schematic illustration of a) super-transus solution treatment in the β field and, b) sub-transus solution treatment in the α-β field, both followed by isothermal aging (adopted from Kolli and Devaraj [19])

Metastable β-titanium alloys are aged to precipitate a second phase and control the mechanical properties. In general, there are four aging methods which are: (1) isothermal aging at low temperature, (2) duplex (two-step) aging, (3) direct aging, and (4) isothermal aging at high temperature. The combination of solution treatment followed by aging will result in the precipitation of α-phase [18,30].

Low-temperature aging is typically conducted between 200 °C and 450 °C. In this temperature range, intermediate metastable phases such as the isothermal ω phase or the β' phase form. These metastable phases cause embrittlement of the alloy but they serve as heterogeneous nucleation sites for the equilibrium α phase, leading to long aging times to complete the transformation to the equilibrium α and β phases [18].

Duplex or two-step aging is performed to control the size and distribution of the α-phase [18]. Figure 7 presents an example of Ti-3.5Al-5Mo-4V microstructure after ST and double aging, showing α-plates in a β matrix and α-grain boundary.

Figure 7 Ti-3.5Al-5Mo-4V microstructure after solution treatment and double aged for 2 h at 300 °C and 500 °C for 8 h (adapted from Ji et al. [31])

Direct aging is when the β-titanium alloy is aged without prior ST. In general, this is performed after the alloy has been cold worked. This process can hinder the formation of the deleterious isothermal ω-phase, while yielding an homogeneous distribution of α-phase precipitates [18].

The high temperature aging is usually done in the temperature range between 500 °C and 600 °C, i.e. above the solvus temperature of the metastable coherent particles ω and β'. When aging metastable β-phase titanium alloys at high temperature, the α-phase nucleates preferentially at β grain boundaries and forms a continuous α-layer. Adjacent to this continuous α-layer is a precipitate free zone (PFZ), which is free of the α-phase [19]. Figure 8 presents β-21S exhibiting grain boundary α-phase in the β-matrix, as well as PFZ after two different aging treatments.

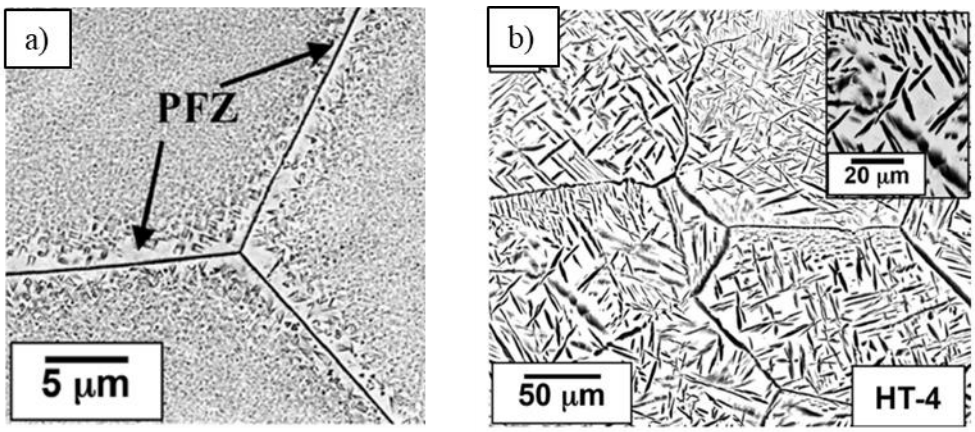

Figure 8 β-21S microstructure after solution treatment at 900 °C for 30 min and water quench (WQ), followed by aging a) 400 °C for 5 h, WQ and 600 °C for 1 h, WQ; and b) 690 °C for 8 h, furnace cooled (FC) and 640 °C for 8 h, FC presenting α-phase on a β-matrix and PFZ (adapted from Mantri et al. [27])

2.2.1 Mechanical properties of heat treated β-21S

To achieve a balance of strength and ductility at room temperature, β-21S is commonly subjected to the basic processing route for metastable β-titanium alloys, consisting of solution treatment, followed by aging in the α+β phase field to precipitate the α-phase [19].

The reported mechanical properties for wrought ST β-21S are presented on Table 1. Since β-21S is normally attractive for high temperature applications, it is worth to mention that this alloy should not be used at elevated temperatures in the ST condition. The elevated temperatures can result in precipitation of a second phase, which will affect the mechanical properties [23].

Table 1 Mechanical properties at room temperature of β-21S after ST (845-850 °C)

Property	Value	References
% elongation	9 - 15	[32-34]
YS (MPa)	834 - 938	[32,33]
UTS (MPA)	862 - 986	[21,32-34]

Figure 9 presents reported microstructures of β-21S after different ST above T_β. These microstructures consist of recrystallized β-phase[26,35].

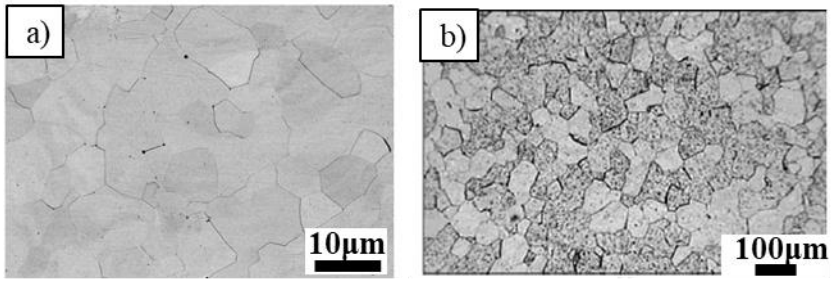

Figure 9. β-21S microstructures presenting recrystallized β-grains after different solution treatments: a) at 870 °C (adapted from Xu et al. [35]) and, c) at 845 °C (adapted from Agarwal et al. [26])

It has been reported in the literature that after solution treatment at 845 °C for 30 min and aging at 540 °C for 8 h, both with air cooling, wrought β-21S will exhibit a microstructure consisting of primarily β-phase, with small precipitation of α-phase as presented in Figure 10.

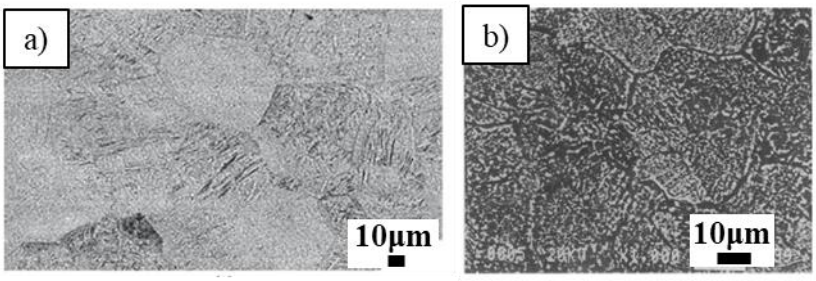

Figure 10 β-21S microstructure after solution treatment 30 min at 845 °C followed by aging 8 h at ~540 °C: a) adapted from Agarwal et al. [26], b) adapted from Huang et al. [36]

The reported mechanical properties of wrought β-21S after STA (ST 845-850 °C and 540 °C) at 25 °C and 450°C are presented in Table 2.

Table 2 Mechanical properties of β-21S after STA (ST 845-850 °C and A 540 °C)

Property	At 25 °C	At 450 °C	References
% elongation	6.5 - 10	7 - 10	[32,33]
YS (MPa)	1100 - 1379	776 - 856	[32,33]
UTS (MPA)	1179 - 1438	909 - 967	[32,33]

2.3 Heat treatment of laser powder bed fusion metastable β-titanium alloys

The properties of titanium alloys can be tailored and homogenized by heat treatments. Since LPBF is a relatively new technique that produces microstructures that differ from traditional methods, the response to heat treatments may also differ. Therefore, the study of heat treatments for alloys fabricated through LPBF is necessary to achieve the control of the properties, according to the pursued applications. For the aerospace industry, titanium alloys are attractive due to their low density, high strength, excellent hardenability, and stability at high temperature. Such properties can be obtained after heat treatment.

As previously discussed, the AM microstructure of metastable β-titanium alloys consists of β-columnar grains in the AB condition and will precipitate the α-phase after aging. The distribution and morphology of α-precipitates will depend on the imposed thermal schedule as well as the alloy composition. Today, there are no studies concerning the heat treatment of LPBF β-21S, this section will explore different heat treatments performed for AM metastable β-titanium alloys and the reported findings.

Bermingham et al. [37] studied the microstructural response to heat treatment and mechanical properties of the metastable β-titanium alloy Ti–3Al–8V–6Cr–4Mo–4Z produced through wire arc AM. Before aging, the alloy was primarily composed of the β-phase, assessed by XRD analysis. After double aging, the α-phase precipitated was observable by Scanning Electron Microscope (SEM) and detected by XRD. After aging at 300 °C for 8 h followed by second aging at 450 °C, a uniform dispersion of fine lenticular α-precipitates developed, as shown in Figure 11 a). The α-precipitates maintained a dense, uniform distribution, exhibiting a lath-like morphology and an increase in size after increasing the second ageing to 525 °C as shown in Figure 11 b). Deng et al. [38] studied the Ti-5Al-5Mo-5V-3Cr-1Zr alloy fabricated by selective laser melting and applied the conventional heat treatment for this alloy. The β phase was identified by XRD and its columnar morphology was identified by Optical microscope (OM) and SEM in the AB condition. After aging at 650 °C for 6 h, precipitation of α-phase was detected by XRD and α-grain boundary and α-plates within β-grains were seen by SEM as can be seen in Figure 11 c-d). Another example is reported for the metastable β-titanium alloy Ti-6Nb-5Al-5Mo-3Cr-0.5Fe. Da Costa et al. [39] studied this alloy manufactured by laser surface melting and aged at 600 and 800 °C, as presented in Figure 11 e) and f), respectively. α-plates were seen by SEM.

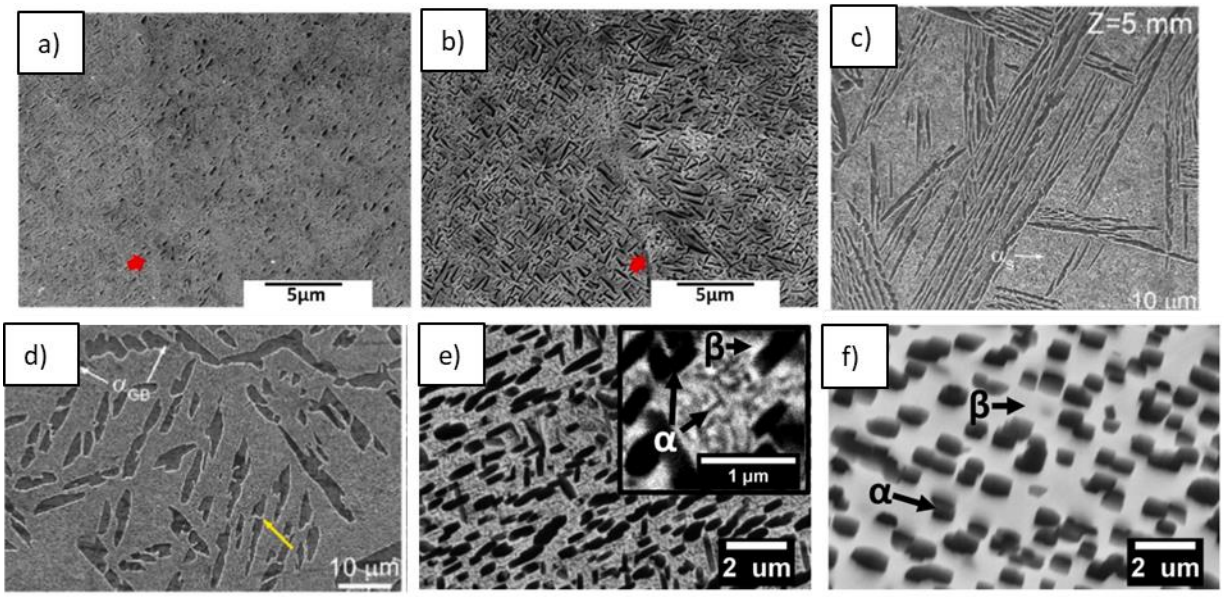

Figure 11 Different metastable AM β-alloys after STA: a-b) Ti–3Al–8V–6Cr–4Mo–4Z (adapted from Bermingham et al. [39]) c-d) Ti-5Al-5Mo-5V-3Cr-1Zr (adapted from Deng et al. [38]) e-f) Ti-6Nb-5Al-5Mo-3Cr-0.5Fe (adapted from Da Costa et al [39])

In agreement with the α-precipitation after aging, the alloys presented an increase in yield strength and a reduction in elongation as can be seen in Table 3.

Table 3 Mechanical properties of different β-titanium alloys produced by AM and heat treated

Alloy	YS (MPA)	% elongation	YS (MPA)	% elongation	Heat treatment	Reference
	AB		After STA			
Ti–3Al–8V–6Cr–4Mo–4Zr	860	45	1210-1385	21-27	ST 850 °C, 30 min and Aging 300 °C, 8 h + aging 450 °C/525 °C	[37]
Ti-5Al-5Mo-5V-3Cr-1Zr	804	~16	1200-1287	4-5	ST 790-880 °C and aging 600, 6 h	[38]

2.4 Laser powder bed fusion of metastable β-titanium alloys

AM of metastable β-titanium alloys has been attracting the attention of scientists since it offers significant advantages in terms of design freedom and cost [40,41]. Focus is being held on obtaining a fully dense structure free of defects as well as studying the microstructure and mechanical properties obtained.

In this section, the literature review of metastable β-titanium alloys produced by LPBF will be explored. Emphasis is given on the solidification process, including the characteristic molten pools, the microstructure and crystallographic orientation obtained after LPBF.

2.4.1 Laser powder bed fusion microstructure of metastable β-titanium alloys

The solidification process experienced during LPBF differ from traditional methods, therefore, it is important to study the microstructure obtained after the high cooling rates experienced during LPBF. The following sections describe useful analyses to understand the solidification process of LPBF metastable β-titanium alloys, starting with the solidification process description and followed by identification of phases present after LPBF.

2.4.1.1 Solidification

The solidification microstructure developed during AM is dominated by epitaxial growth of crystals [42], causing a columnar grain microstructure observed in AM alloys such as steels,

Inconel 718, and Ti-6Al-4V. It is commonly found that the microstructure in the columnar grains will be strongly textured with some stray grains [3].

When looking at a face parallel to the BD using OM or SEM, it is possible to observe the characteristic molten pool shape found in LPBF alloys. The geometrical features of the melt pool are determined in a complex way by several LPBF process parameters, mainly laser power, laser scan speed, and scan strategy, as well as the choice of the powder size distribution and powder bed thickness.

The solidification kinetics will determine the melt pools [43], and define the characteristics of the solidifying structure. Commonly, β-grains grow from the boundary toward the center of the melt pool along the maximum heat flow direction, which is perpendicular to the solidifying surface of the melt pool [15]. The resulting microstructure, including texture, grain size, and morphology, as well as density and size distribution of precipitates, is intimately affected by the thermal profile experienced in the solidifying melt pool [15]. Figure 12 presents examples of different shapes presented for molten pools of three metastable β-titanium alloys. Elongated β-grains are visible growing across molten pool boundaries.

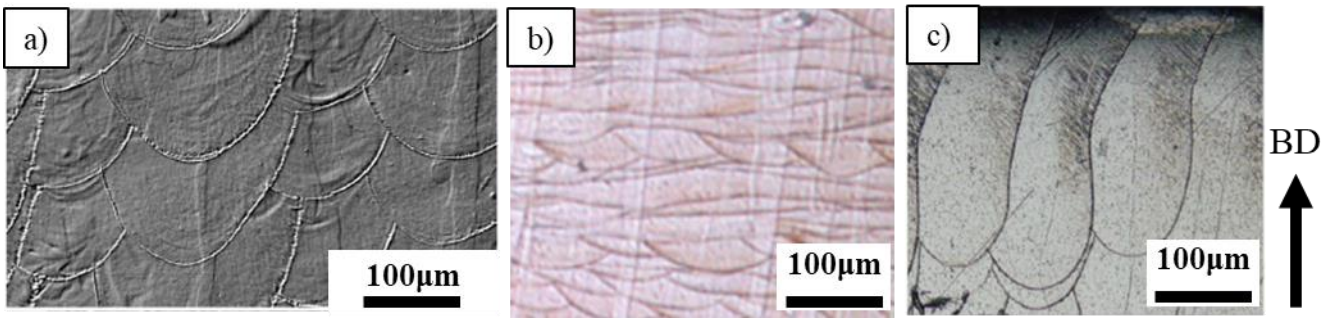

Figure 12 Molten pool shape presented for metastable β-titanium alloys a) Ti-Cr (adapted from Nagase et al. [44]), b) β-21S (adapted from Pellizari [45]), c) Ti-15Mo-5Zr-3Al (adapted from Nakano et al. [41])

Inside each molten pool, the formation of dendrites can be observed by SEM. Dendrites identified inside the LPBF Ti–5Al–5V–5Mo–3Cr–0.5Fe can be seen in Figure 13. The dendritic structure grown perpendicular to the melt pool boundaries, aligned with the highest temperature gradient direction. These dendrites can be further analyzed to obtain the preferred crystallographic orientation as will be discussed in the next section.

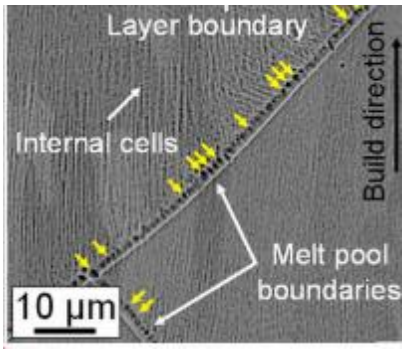

Figure 13 SEM images presenting the parallel orientation on the surface dendrites respect to the <100> crystallographic direction on LPBF Ti–5Al–5V–5Mo–3Cr–0.5 Fe (adapted from Zafari et al. [46])

2.4.1.2 Crystallographic orientation

The preferred orientation of the dendrites can be analyzed by electron backscatter scanning diffraction (EBSD). Figure 14 presents EBSD imaging of metastable β-titanium alloys produced by LPBF. A cubic structure is well developed as the standard stereographic projection of the cubic crystal as shown in the pole figures presented in Figure 14 b) and d), and corresponds to the orientation {001}<100>. In this case, the plane (001) of the family of planes {100} is parallel to the construction surface thus perpendicular to the building direction and the pole figure presents a direction [001] parallel to the building direction. The growth direction of the dendrites will be determined by the crystal structure; BCC and FCC structures possess a preferred <100> crystallographic direction. Since the β-metastable titanium alloys have a BCC structure, dendrites in these alloys preferentially grow along the six equivalents <100> orientations [47], and this growth direction generally matches with the building direction.

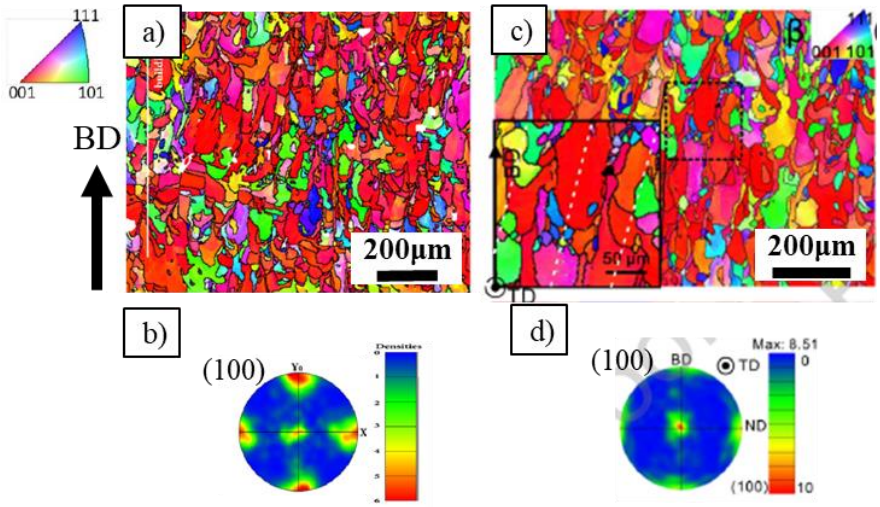

Figure 14 EBSD phase maps and pole figures of AM metastable β-titanium alloys: a)-b) Ti–26Nb (adapted from Fischer et al. [48]), c)-d) Ti-12Mo-6Zr-2Fe (adapted from Duan et al. [49])

2.4.1 Phases of laser powder bed fusion metastable β-titanium alloys

Typical microstructure of metastable β-titanium alloys fabricated by AM consists of a β-phase matrix. In some cases, a small percentage of second phases such as α- or ω-phases can also be found.

X-Ray diffraction (XRD) is a rapid analytical technique that can be used for phase identification of a crystalline material. Figure 15 presents the XRD obtained for the SLM produced alloy Ti-6Al-4V Eli +10Mo reported by Vrancken et al. [50] They studied the as-built alloy and its evolution after different heat treatments. They found only the β-phase in the as-built condition and found precipitation of the α-phase after different aging (at 650, 850, 900 and 1050 °C) identifying the phases by XRD and SEM.

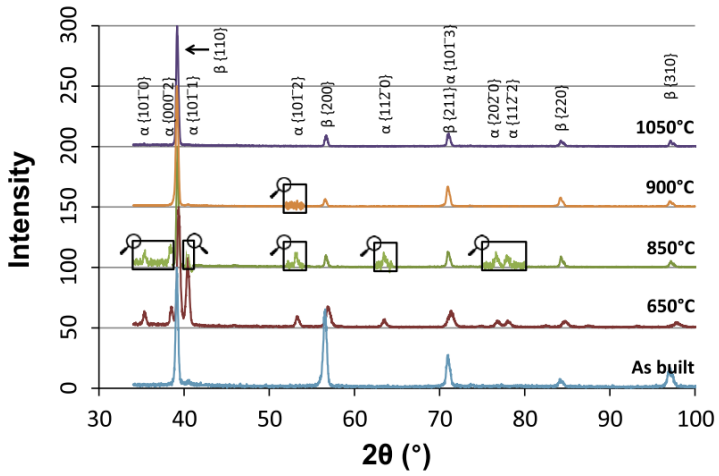

Figure 15 XRD of SLM Ti-6Al-4V Eli +10Mo as built and after different heat treatments (adapted from Vrancken et al. [50])

SEM is useful to confirm the phases present in an alloy and observe its morphology. Figure 16 presents a cross-sectional view of SEM micrographs of Ti-5Al-5V-5Mo-3Cr and Ti-26Nb, two different metastable β-titanium alloys produced by LPBF, showing β-grains presented after the LPBF process. The morphology presented of the β-grains depends on the solidification process and will be further discussed in the next section.

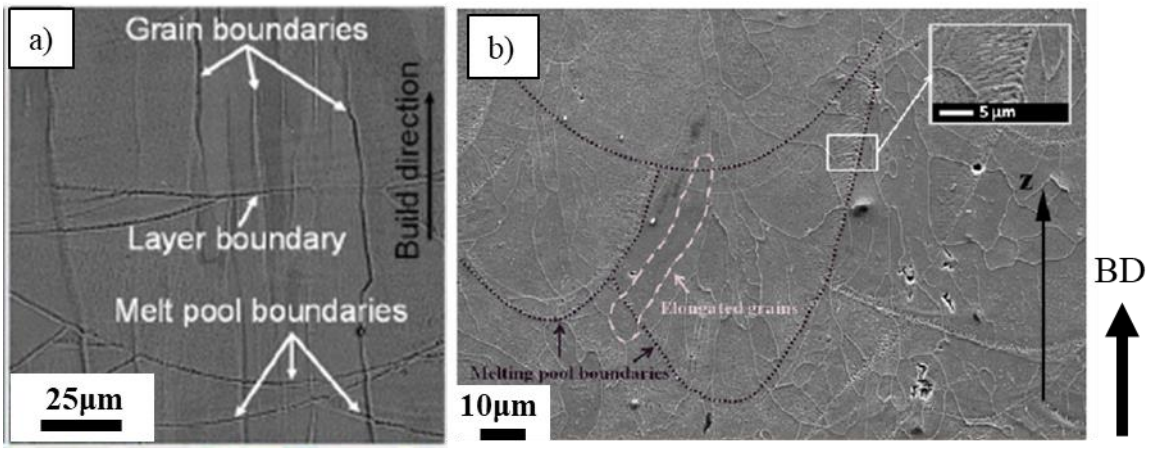

Figure 16 Microstructures observed in AM metastable β-titanium alloys: a) Ti-5Al-5V-5Mo-3Cr (adapted from Zafari et al. [46]) b) Ti–26Nb (adapted from Fischer [48])

2.4.2 Laser powder bed fusion of Titanium β-21S

Nowadays, there is limited information on AM of β-21S. Perrizalli et. al. [45] reported β-21S produced by LPBF with optimized parameters to obtain a preferred <100> crystallographic

direction on the β-grains. They presented a near fully dense alloy (99.75 %) with columnar β-phase parallel the BD. The reported microstructure and pole figures are presented in Figure 17.

The reported mechanical properties were a Young's modulus of 52 GPa. Mechanical strength $\sigma_{y0.2}$ of 709 MPa, UTS = 831 MPa and high total elongation during tensile test (21%).

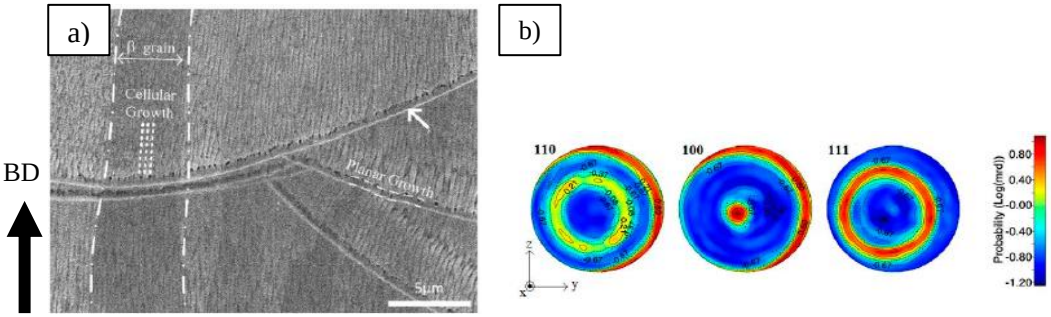

Figure 17 LPBF β-21S a) SEM micrograph presenting columnar β grains along the building direction b) pole figures presented (adapted from Pellizari et al. [45])

As can be seen, limited information exists in the literature about metastable β-titanium alloys. There is no information related to the heat treatment of LPBF β-21S. This limitation has been addressed in the present thesis by applying the standard heat-treatment to LPBF β-21S, relating the mechanical properties to the microstructure. In addition, the mechanical properties of LPBF β-21S at elevated temperature has been reported for the first time.

2.5 Fracture surface of metastable β-titanium alloys

The fracture mode varies according to the fracture mechanism that corresponds to the microstructure presented on the alloy. Metastable β-titanium alloys produced by AM are characterized by exhibiting a ductile dimpled fracture when exhibiting primarily β-phase. This feature may depend on the morphology of the β-phase. Deng et al. [38] presented the SEM fracture surface of the above-mentioned Ti-5Al-5Mo-5V-3Cr-1Zr fabricated by AM. Figure 18 a) presents the microstructure consisting on elongated β-grains. Figure 18 b) presents the fracture of the as-fabricated alloy, identified by SEM, presenting a ductile dimpled fracture. Qiu et al. [51] also presented the SEM fracture of the β-titanium alloy Ti-10V-2Fe-3Al, after SLM. They explored different printing parameters and found a microstructure consisting of β-grains in elongated and equiaxed shapes. In agreement with Deng's study, Figure 18 c) presents the samples which

consisted of β-elongated grains and presented numerous fine dimples after fracture, indicating the ductile nature of this sample as can be seen in Figure 18 d).

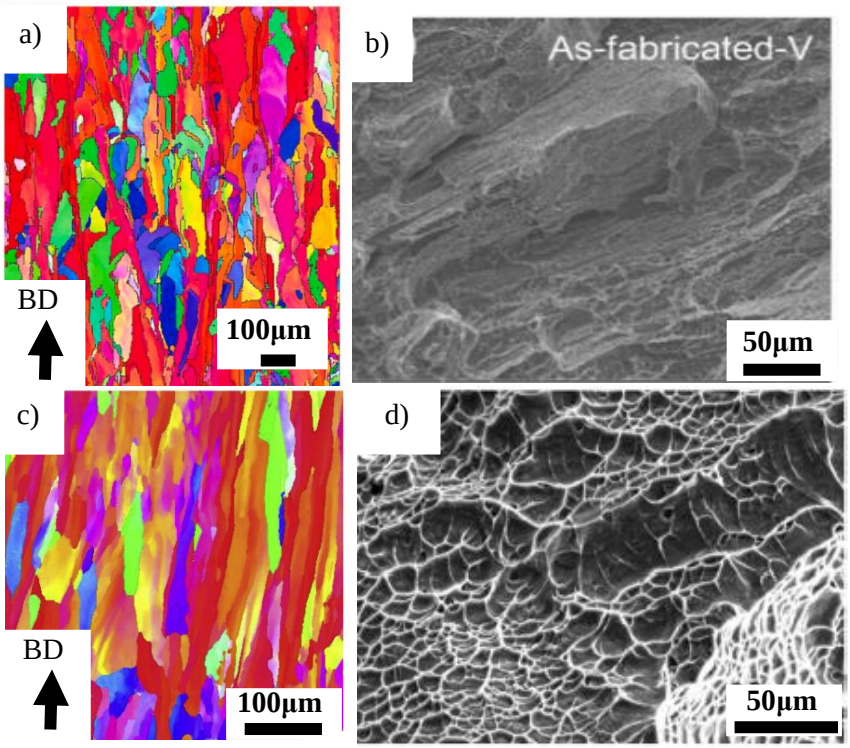

Figure 18 a-b) AB Ti-5Al-5Mo-5V-3Cr-1Zr presenting ductile fracture (adapted from Deng et al. [38]); c-d) AB Ti-10V-2Fe-3Al presenting ductile fracture of β-elongated grains (adapted from Qui et al. [51])

However, the sample containing a lot of equiaxed grains as presented in Figure 19 a) failed in an intergranular fracture mode as can be seen in Figure 19 b). In that sample, the grain boundaries were acting as the weak link. Some dimples were also observed on the fracture surface of the same sample as can be seen in Figure 19 c) suggesting that certain localized plasticity was present.

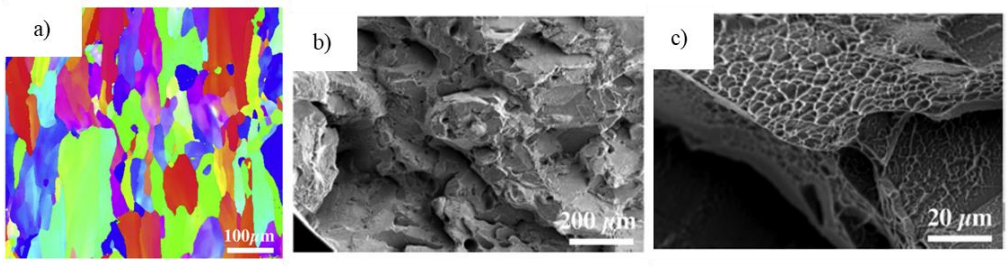

Figure 19 Ti-10V-2Fe-3Al a) EBSD b) intergranular fracture of β-equiaxed grains c) localized plasticity of the β-equiaxed grains

The mechanical properties and fracture mechanisms of titanium alloys with α+β microstructures are heavily influenced by the size of the α-precipitates, the continuity of the α-grain boundary layer and the spatial arrangement of these phases [25,19,38]. In general, the α+β microstructures present low work-hardening rate, which promotes easier void growth, resulting in ductile fracture at relatively low strains. However, low ductility intragranular fracture may also occur when there is continuous α-grain boundary present along with high precipitation of α-intergranular.

To explore the different influence of the α-phase morphology, Figure 20 presents three different microstructures and surface fractures found by Deng's et al. [38] for the AM Ti-5Al-5Mo-5V-3Cr-1Z after different STA. The microstructure presented in Figure 20 a) consisted of massive precipitation of intragranular α-plates within the β-matrix along with continuous α-grain boundary. After mechanical testing, this sample presented a typical brittle faceted fracture mode, indicating that the crack propagation occurred in an intergranular form along the continuous α-grain boundary as can be seen in Figure 20 b). On the other hand, structures consisting of α-lamellae and discontinuous α-grain boundary as can be seen in Figure 20 b-c) resulted in a more ductile fracture mode: a bimodal fracture mode resulted from short thick α-plates as dimples and facets are visible in Figure 20 e)); while completely dimpled ductile fracture resulted from longer, thinner plates as presented in Figure 20 f). Indicating that the continuity of the α-grain boundary plays an important role in the fracture mode, however, the morphology of the intergranular α-phase is also important.

Similarly, Mantri et al. presented a study of wrought β-21S [27] subjected to different heat-treatments. The microstructure consisted of α-grain boundary as well as intergranular α-phase, which was present in the shape of fine precipitates for one sample and larger plates for another, as presented in Figure 21 a) and b), respectively. After mechanical testing, the sample with fine α-precipitation presented bimodal fracture with clear evidence of fracture through grain boundary, as well as dimples as seen in Figure 21 c), while the sample with α-plates only exhibited dimpled fracture, as seen in Figure 21 d), although both samples presented α-grain boundary.

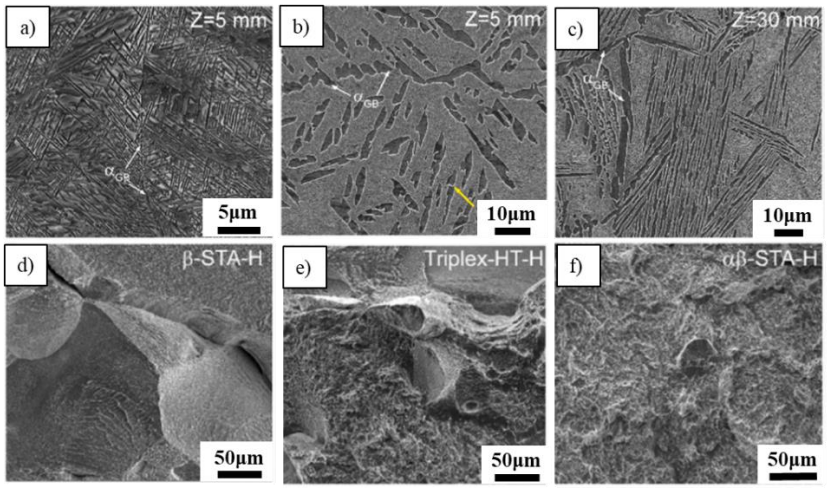

Figure 20 SLM Ti-5Al-5Mo-5 V-3Cr-1Zr a) microstructure b) fracture surface presenting intragranular fracture (adapted from Deng et al. [38])

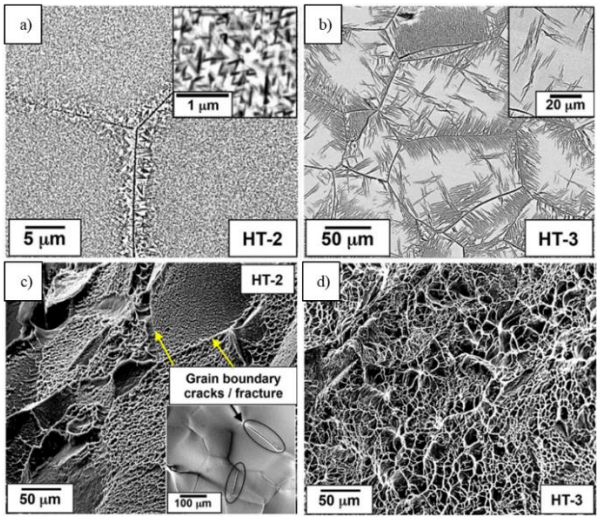

Figure 21 Wrought β-21S presenting different a-d) microstructures and c-h) their respetive surface fracture (adapted from Mantri et al. [27])

Chapter 3 – Experimental Methodology

This chapter will discuss the equipment and procedures used to obtain the results presented in Chapter 4.

3.1 Powder Characterization

The β-21S powder used was sourced from GKN Powder Metallurgy. Table 4 shows the composition as specified by the certificate of conformity provided by the supplier.

Table 4 Chemical composition of β-21S powder from the certificate of conformity of the supplier.

Element	Mo	Al	Nb	Si	O	C	H	N
Wt. %	15	3.2	2.7	0.2	0.17	0.05	0.02	0.05

The powder was analyzed in terms of particle size distribution (PSD), surface morphology and flowability. These techniques and its results will be described in this section.

3.1.1 Particle size distribution

The PSD of the powders was measured using laser particle scattering (LPS) technique. LPS considers the light intensity distribution of scattered laser light from a bulk of solid particles.

Experimental setup and process

For this study LA-920 Horiba laser particle size analyzer was used to measure the PSD. Figure 22 shows the PSD of the powder with a D10, D50 and D90 of 32, 45 and 70 μm, respectively. The powder was mixed prior to characterization to ensure correct measurement. LPS results reported are the average of 3 measurements.

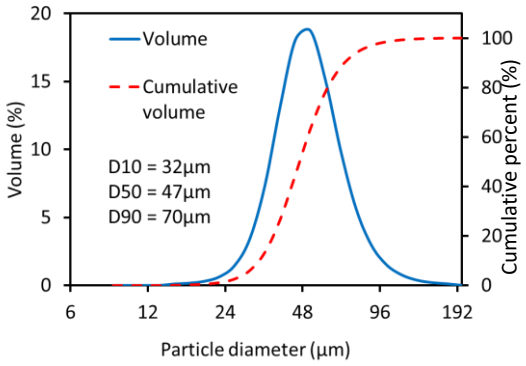

Figure 22 Particle size distribution of Ti β-21S

3.1.2 Surface Morphology

SEM was used to analyze particle surface morphology. A SEM Hitachi SU3500 microscope was used. Secondary electron images of the powders were collected at an accelerating voltage of 20 KeV.

3.1.3 Flowability

Powder flowability measurements were conducted on a hall flowmeter apparatus. Measurements were conducted per ASTM B212-3. 50 g powder samples were loaded into the funnel. In this technique, the time that takes the entire powder to flow through the funnel is measured. Flowability of the powder was reported as the time per mass "s/50 g" for each powder. To ensure repeatability, measurements are reported as the average of 3 runs.

Experimental setup and process

Powder flowability analysis was conducted by using a GranuDrum apparatus shown on Figure 23. The cohesive index (CI) value is as a function of rotational speed is shown in Figure 24. The measured values ranged between 13-19 for rotating speeds up to 30 rpm. Literature has shown that powder with lower cohesive index possesses better flowability [52], with a critical CI of 24 to maximize powder spreading quality for powder bed processing [52].

Figure 23 GranuDrum apparatus

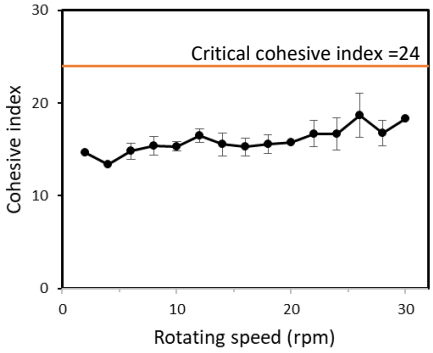

Figure 24 Cohesive index of Ti β-21S

3.2 LPBF manufacturing

Experimental setup and process

All the samples were manufactured using a Renishaw AM400 LPBF machine equipped with a 400 W pulsed Nd:YAG presented in Figure 25. To prevent oxidation, the process was conducted under Ar atmosphere, and the O_2 was kept below 300 ppm throughout the print. Ti-6Al-4V (wt. %) standard set of parameters provided by Renishaw were used with scanning strategy of 67° rotation per layer for Chapter 4.

Figure 25 Renishaw AM 400

3.3 Metallurgical Characterization Techniques

3.3.1 Metallographic Specimen preparation

Samples were sectioned with a saw machine then hot mounted in bakelite. Samples were ground with 600, 800, and 1200 grit SiC grinding paper, then polished using 0.05 µm polishing pad and a solution of 10 ml of silica suspension, 150 ml of hydrogen peroxide and 440 ml of water. Final polishing was conducted using a Buehler Vibromet 2 vibratory polisher with silica suspension. Samples were thoroughly rinsed and dried prior to characterization activities. The selected planes for analysis are depicted in Figure 26. The microstructure was revealed when needed using Kroll's etchant (91 % deionized water (H_2O), 6 % nitric acid (HNO_3) and 3 % hydrofluoric acid (HF)).

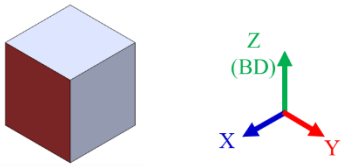

Figure 26 Schematic illustrations of the plane used for microstructural analyses for Chapter 4

3.3.2 Optical Microscopy

All the samples were optically imaged after etching to analyze molten pool obtained, porosity and microstructure.

For optical imaging, a Nikon light OM equipped with a Clemex Vision System was used. This OM is presented in Figure 27.

Figure 27 Nikon light optical microscope

3.3.3 Analysis software

The relative density as well as the volume percentage of the α-phase was obtained using image analysis software Image J [53].

3.3.4 Experimental density

Experimental density was measured by the Archimedes' principle.

Archimedes' Principle

Archimedes' Principle or physical law of buoyancy, states that any body completely or partially submerged in a fluid (gas or liquid) at rest is acted upon by an upward, or buoyant force, the magnitude of which is equal to the weight of the fluid displaced by the body. The volume of displaced fluid is equivalent to the volume of an object fully immersed in a fluid or to that fraction of the volume below the surface for an object partially submerged in a liquid. The weight of the displaced portion of the fluid is equivalent to the magnitude of the buoyant force. The buoyant force on a body floating in a liquid or gas is also equivalent in magnitude to the weight of the floating object and is opposite in direction [54].

Experimental setup and process

The sample weight was first measured in air to obtain their mass. Then, in isopropanol to obtain the apparent mass when submerged. This measurement allows the calculation of the sample's volume by Equation (2):

Mass of object – apparent mass when submerged = Density of isopropanol * Volume of object (2)

The volume of the object can be then calculated by Equation (3):

$$\text{Volume} = \frac{\text{Mass of sample in air – apparent mass when submerged in isopropanol}}{\text{Density of isopropanol}} \quad (3)$$

$$\text{Volume} = \frac{1.8715\ \text{g} - 1.5726\ \text{g}}{0.786\ \text{g/cm}^3} = 0.38\ \text{cm}^3$$

Then, the density can be calculated by Equation (4):

$$\rho = \frac{\text{mass}}{\text{volume}} \quad (4)$$

3.3.5 X-Ray Diffraction

Phase analysis was performed by XRD.

Experimental setup and process

Phase analysis was conducted for both, AB and STA samples, using a Bruker D8 Discovery X-Ray Diffractometer (XRD) with a copper source (λ =1.5406 nm) as the one presented on Figure 28. The XRD was performed in the range of 20-100° in 2 Θ using 4 frames and 300 s per frame.

Figure 28 Bruker D8 Discovery XRD

3.3.6 Scanning Electron Microscopy

SEM was used to study microstructural and fractography features.

Experimental setup and process

Microstructural and fractography analysis were conducted on the tested samples with a Hitachi 3500 SEM, presented in Figure 29.

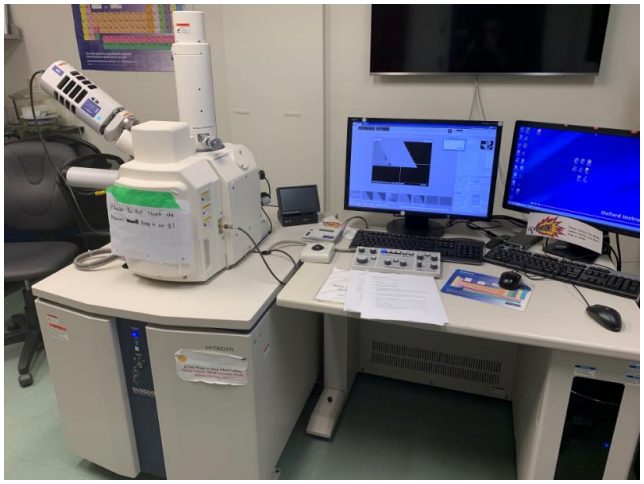

Figure 29 Hitachi 3500 SEM

3.3.7 Backscattering Electron Microscopy

Grain morphology, texture, and phase map in the AB condition were analyzed by electron backscattered diffraction (EBSD)

Experimental setup and process

EBSD was done using a Hitachi SU3500 SEM prior to etching. The operating conditions were 15 kV and 0.2 μm step size. Aztec data acquisition software combined with the HKL Channel 5 data processing software was used for the EBSD data analysis.

3.3.8 Energy Dispersive Spectroscopy

Phase composition was analyzed using energy dispersive spectroscopy (EDS)

Experimental setup and process

A Hitachi 3500 SEM equipped with EDS was used for detailed microstructural analysis of the heat-treated specimen.

3.3.9 Post processing heat treatment

The heat treatment of Chapter 4 consisted of a β-solution treatment at 850°C (above β-transus, ~805°C [29]) for 0.5h, air cooled (AC); then aged at 538°C for 8h followed by AC. A schematic representation of the heat treatment schedule is presented in Figure 30.

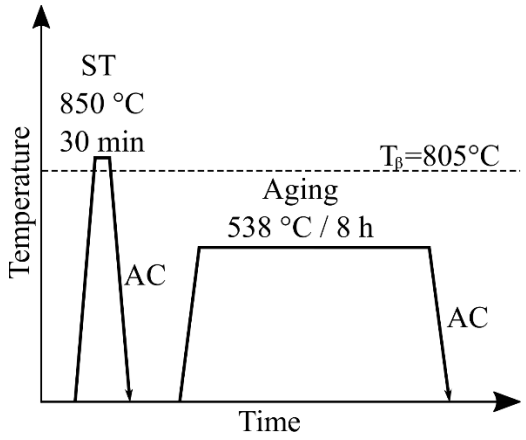

Figure 30 Schematic of the heat treatment tested in this study

3.3.10 Mechanical properties

For Chapter 4, Vickers microhardness and tensile test were performed.

Experimental setup and process

Vickers microhardness analysis was performed on a CM-100AT Clark microhardness indenter using 200 gf load and a dwell time of 15 s. Ten independent measurements were done within each sample and averaged.

Tensile tests for Chapter 4 were carried out at RT and at 450 °C using a TestResources 313Q electromechanical test machine with a constant crosshead speed (0.75 mm/min), resulting in a strain rate of 6.7 ×10-4 s-1 (gauge length of 12.5 mm). The selected elevated testing temperature was 450 °C as the recommended continuous operating temperature for Ti β-21S is 480 °C [26].

Chapter 4 – Microstructure and mechanical properties of β-21S Ti alloy fabricated through laser powder bed fusion

4.1 Preface

Chapter 4 is a manuscript published in Progress in Additive Manufacturing (Springer Nature, Switzerland). The citation information is provided as follows:

Macias-Sifuentes MA, Xu C, Sanchez-Mata O, Kwon SY, Atabay SE, Muñiz-Lerma JA, Brochu M (2021) Microstructure and mechanical properties of β-21S Ti alloy fabricated through laser powder bed fusion. Progress in Additive Manufacturing. doi:10.1007/s40964-021-00181-7

Chapter 4 evaluates the manufacturability of β-21S by LPBF and the effect of post heat-treatment, to understand the relationship between the microstructure and the mechanical properties of this alloy.

4.2 Abstract

Metastable β-titanium alloys are attractive for their high strength-to-density ratio, good hardenability, excellent fatigue behavior, and corrosion resistance. Among these alloys, β-21S, with a composition of Ti-15Mo-3Nb-3Al-0.2Si (wt. %), is known to offer improved elevated temperature strength, creep resistance, thermal stability, and oxidation resistance. In this study, laser powder bed fusion (PBF-LB) of β-21S and the effect of post-PBF-LB heat treatment was investigated to understand the relationship between the microstructure and the mechanical properties. The as-built (AB) alloy is primarily composed of β-phase, with columnar grains oriented along the build direction. The alloy AB presented a microhardness of 278 HV, a yield strength (YS) of 917 MPa, an ultimate tensile strength (UTS) of 946 MPa, and a ductility of 25.3 % at room temperature (RT). Such properties are comparable to β-21S in solution treatment (ST) condition. Solution treatment and aging (STA) of the alloy precipitated the α-phase, increasing the microhardness to 380 HV, YS to 1281 MPa and UTS to 1348 MPa, while reducing the ductility to 6.5 % at RT. The STA alloy presented a YS of 827 MPa, UTS of 923 MPa, and a ductility of 7.7 %, at 450 °C. The thermal treatment applied to PBF-LB β-21S had a similar effect compared to β-

21S fabricated by non-AM techniques. The properties obtained demonstrate that β-21S is a potential candidate for AM.

4.3 Introduction.

AM is emerging as a complementary route to the traditional manufacturing processes to fabricate high complexity components. PBF-LB, one of the most studied process among metal AM, uses powder feedstock which is selectively melted by a focused laser to form a characteristic part after melt pool solidification [1-4]. PBF-LB has raised attention due to its high degree of manufacturing freedom, its ability to produce lightweight intricate components [5,6], and its energy-efficient, and time saving route [6,7].

Metastable β-titanium alloys are attractive materials for aerospace applications due to their high strength-to-density ratio, good hardenability, excellent fatigue/crack-propagation behavior capabilities with processes such as cold strip rolling [8,9]. Compared to other metastable β-titanium alloys, β-21S offers better oxidation resistance, it can retain its strength at higher temperatures [10,9,11], and has increased corrosion resistance [10,12]. β-21S is an age hardenable metastable β-titanium alloy that has great forming capabilities, contains a balance of β-stabilizers which upon fast cooling from above β-transus, retains the β-phase [8,13], and the formation of martensite at room temperature is inhibited. The β-phase retained is metastable at high temperature and is typically heat treated to precipitate the α-phase, to increase the strength and stabilize the microstructure of the alloy. Typical heat treatment involves solution treatment at temperatures above the β-transus (805°C [14]) (known as β-solution treatment) followed by aging [8]. Aging at temperatures above the ω-solvus (350°C [15]) will precipitate the α-phase within the grains and at the grain boundaries [13,16] strengthening the alloy [17]. The selected heat treatment in this study is the standard STA for β-21S [18] with aging temperature above the ω-solvus. Agarwal et al. [19] and Huang et al. [4] studied the influence of different heat treatments on the microstructure of β-21S produced by non-AM processes in STA. With the standard heat treatment used in this study, they reported a microstructure consisting on fine α-phase in a β-matrix and on the grain boundaries. Huang et al. reported the α-phase is expected to precipitate with a volume percentage ranging between 20-33 % [4].

Although many studies have focused on PBF-LB of titanium alloys [5,7,20], there is limited information on PBF-LB of β-21S and its response to post-process heat treatment. Pellizari et al. [21] reported near fully dense PBF-LB β-21S, consisting on elongated β-phase with UTS of 831 MPa and 21 % elongation and no heat-treatment study was conducted. To fill this knowledge gap, in this research, the mechanical behavior of the AB and STA β-21S alloys produced by PBF-LB was investigated. Tensile properties and hardness were measured for both alloys. The resulting mechanical properties conducted at RT and at 450°C were correlated with the microstructure, assessed by scanning electron microscopy (SEM), and optical microscope (OM).

4.4 Materials and methods.

β-21S powder, sourced from GKN Powder Metallurgy, was used. Table 5 shows the composition as specified by the certificate of conformity provided by the supplier.

Figure 31 shows the powder morphology that was mostly spherical with a few satellites. The particle size distribution (PSD) was measured by using LA-920 Horiba laser particle size analyzer. Figure 32 (a) shows the PSD of the powder with a D10, D50 and D90 of 32, 45 and 70 µm, respectively. Powder flowability analysis was conducted by using the GranuDrum apparatus. The cohesive index (CI) value is as a function of rotational speed is shown in Figure 32 (b). The measured values ranged between 13-19 for rotating speeds up to 30 rpm. Literature has shown that powder with lower cohesive index possesses better flowability [22], with a critical CI of 24 to maximize powder spreading quality for powder bed processing [22].

Table 5 Chemical composition of β-21S powder from the certificate of conformity of the supplier.

Element	**Mo**	**Al**	**Nb**	**Si**	**O**	**C**	**H**	**N**
Wt. %	15	3.2	2.7	0.2	0.17	0.05	0.02	0.05

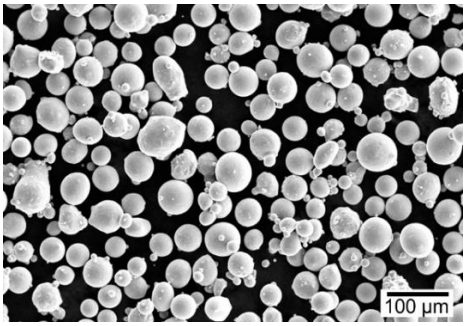

Figure 31 SEM micrographs showing the size, shape and morphology of the β-21S particles

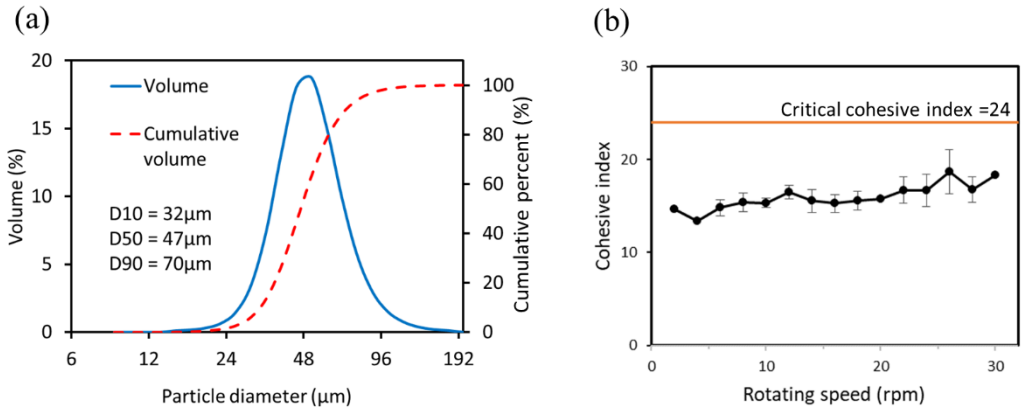

Figure 32 (a) Particle size distribution and (b) cohesive index of Ti β-21S

Rectangular prism samples with dimensions of 80 mm × 10 mm × 10 mm were manufactured using a Renishaw AM400 PBF-LB machine equipped with a 400 W pulsed Nd:YAG. To prevent oxidation, the process was conducted under Ar atmosphere, and the O_2 was kept below 300 ppm throughout the print. Ti-6Al-4V (wt. %) standard set of parameters provided by Renishaw were used with scanning strategy of 67° rotation per layer.

The heat treatment consisted of a β-solution treatment at 850°C (above β-transus, ~805°C [14]) for 0.5h, air cooled (AC); then aged at 538°C for 8h followed by AC. A schematic representation of the heat treatment schedule is presented in Figure 33.

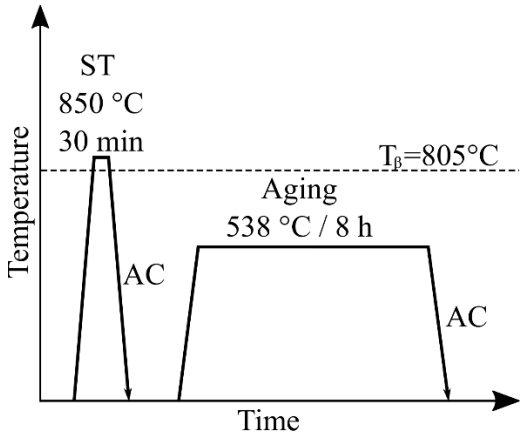

Figure 33 Schematic of the heat treatment tested in this study

Phase analysis was conducted for both, AB and STA samples, using a Bruker D8 Discovery X-Ray Diffractometer (XRD) with a copper source (λ =1.5406 nm). The XRD was performed in the range of 20-100° in 2 Θ using 4 frames and 300 s per frame. The AB and STA samples were sectioned along the build direction (BD) for microstructural examination and prepared following a standard metallographic procedure. Grain morphology, texture, and phase map in the AB condition were analyzed by electron backscattered diffraction (EBSD) system using a Hitachi SU3500 SEM. The operating conditions were 15 kV and 0.2 μm step size. Aztec data acquisition software combined with the HKL Channel 5 data processing software was used for the EBSD data analysis. The microstructure was revealed using Kroll's etchant (91 % deionized water (H_2O), 6 % nitric acid (HNO_3) and 3 % hydrofluoric acid (HF)). For optical imaging, a Nikon light optical microscope (OM) equipped with a Clemex Vision System was used. The relative density as well as the volume percentage of the α-phase was obtained using image analysis software Image J [23]. Experimental density was measured by the Archimedes' principle. A Hitachi 3500 SEM equipped with energy dispersive spectrometer (EDS) was used for detailed microstructural analysis.

Vickers microhardness analysis was performed on a CM-100AT Clark microhardness indenter using 200 gf load and a dwell time of 15 s. Ten independent measurements were done within each sample and averaged. Tensile tests were carried out at RT and at 450 °C using a TestResources 313Q electromechanical test machine with a constant crosshead speed (0.75 mm/min), resulting in a strain rate of 6.7×10^{-4} s^{-1} (gauge length of 12.5 mm). Fractography analysis was conducted on the tested samples with a Hitachi 3500 SEM.

4.5 Results.

4.5.1 Microstructural characterization of AB

The density measurement as well as the microstructure analyses of the AB alloy were carried on a plane parallel to the BD as indicated in the schematic in Figure 34 (a). Figure 34 (b) shows a mosaic of micrographs of an AB sample used to measure the relative optical density through image analysis. An average relative density of 99.9 % was measured. While a density of 4.92 g/cm^3 was obtained using Archimedes' principle, which is 99.8% in relation to the reference density value established for the alloy, 4.93 g/cm^3 [24]. Few near-spherical in morphology and randomly distributed pores, associated to gas entrapment from the shielding Ar gas atmosphere during processing [2] were observed within the sample.

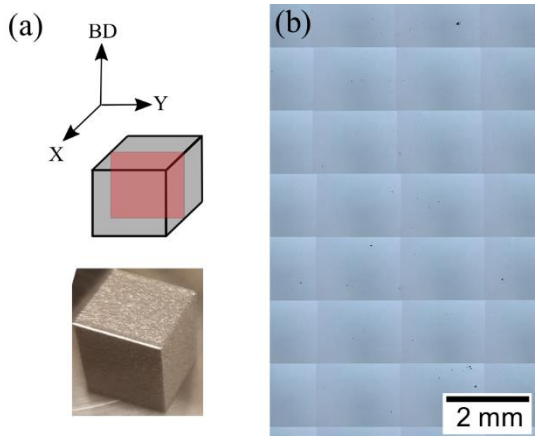

Figure 34 (a) Schematic illustrations of the plane used for microstructural analysis (b) Optical image showing the relative density in AB condition

Figure 35 (a) depicts the XRD pattern of the AB sample. The XRD suggests the presence of a single β-phase, which matches PDF 04-020-9142 [25].

The molybdenum equivalency (MoE) value of 12.84 for β-21S calculated using the Equation (5) [26] supports the observation of a β-phase at RT as reported by Ivasishin et al. [27]. In general, a MoE value of approximately 10.0 is required to stabilize the β-phase when cooling from above the beta transus temperature.

$$MoE = 1.0(wt.\%\ Mo) + 0.67(wt.\%\ V) + 0.44(wt.\%\ W) + 0.28(wt.\%\ Nb) + 0.22(wt.\%\ Ta) + 2.9(wt.\%\ Fe) + 1.6(wt.\%\ Cr) + 1.25(wt.\%\ Ni) + 1.70(wt.\%\ Mn) + 1.70(wt.\%\ Co) - 1.0(wt.\%\ Al) \quad (5)$$

To further confirm this single β-phase, a phase map using EBSD was obtained and shown in Figure 35 (b). The EBSD analysis was performed for BCC and HCP structures, and are represented by blue and red colors, respectively. As shown, the volume fraction of HCP precipitates seems to be extremely low. To get insight on the presence of the precipitates, a continuous cooling transformation (CCT) and isothermal transformation (TTT) diagrams were calculated by TC-PRISMA [28]. Figure 36 presents the CCT and TTT diagrams depicting the onset of α-phase precipitation (volume fraction = 10^{-4}) in the β-phase matrix. Since the alloy has a solidus temperature of 1401 °C/s, and is subjected to cooling rates in the order of 10^3-10^4 °C/s, which are the common cooling rates in the solid state observed during PBF-LB [29], the CCT diagram was calculated below this temperature, and within this range. The theoretical calculation shows that even the fastest cooling rate associated with PBF-LB is not high enough to suppress the precipitation of α-phase when passing through the solvus. The α-phase was measured from the phase map to be 0.27%, it should be noted that α-phase was not detected in Figure 35 (a) due to the small volume.

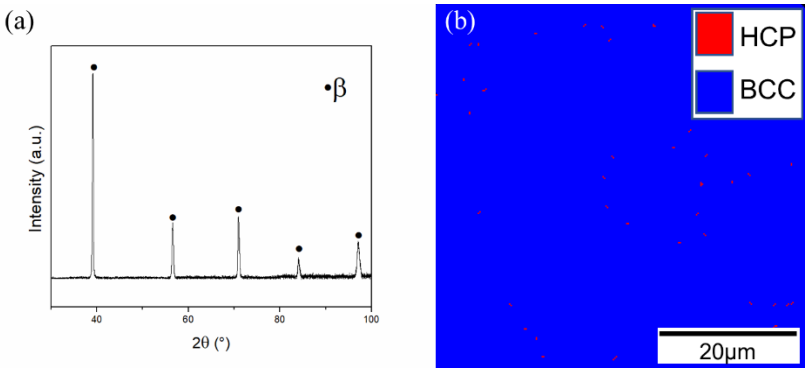

Figure 35 (a) XRD, (b) phase map of the AB sample

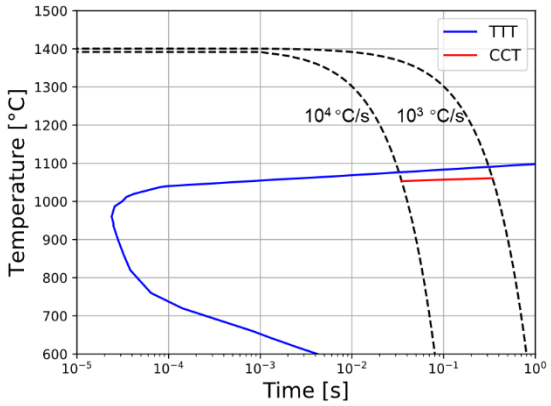

Figure 36 The calculated CCT and TTT diagrams for β-21S. Blue line: TTT diagram, red line CCT diagram for α-phase with volume fraction of 10^{-4}. Dashed lines indicate the cooling rates 10^4 °C/s and 10^3 °C/s

In order to analyze the microstructure, the samples were observed under OM and SEM after etching. Figure 37 (a) presents an optical micrograph of the AB sample. Molten pool boundaries are clearly visible in the AB state. Since the remelting of layers during PBF-LB affects the molten pool size, the measurements were taken from the top layer only. The average sizes resultant of the width and depth of the molten pool were 124 ± 15 µm and 70 ± 10 µm, respectively. The presence of β columnar grains with a width of 33 ± 26 µm can also be seen to be primarily parallel to the BD. Formation of columnar microstructure during PBF-LB has been reported before for other Ti alloys [20,30]. During PBF-LB, a large heat flux is created parallel to the BD. The grains grow along the direction of highest thermal gradient [6,31], and thus, aligning with the BD. Each layer partially re-melts the previous layer, facilitating the grain growth from existing grains, which acts as a driving force for crystal growth in the same orientation. The epitaxial growth has been reported before for AM and is well documented in [6,31,32].

Figure 37 (b) shows a SEM micrograph of the same AB sample. The microstructure in the AB state revealed cellular columnar features within the grains that grew across the molten pool boundaries. The cellular sub-grains form parallel to the heat flux, as mentioned before, following the thermal gradients, and perpendicular to the melt pool. Thus, the dendrites grow through epitaxial growth through multiple layers. Mode and size of the solidification structure are influenced by the growth rate R (m/s) and the temperature gradient G (°C/m), which are the main solidification parameters. Equiaxed dendrite growth is favored by a lower G/R ratio, while a

columnar morphology is favored by higher values of G/R. The high thermal gradient and low growth rate associated to PBF-LB (10^6 °C/m and 0.4 m/s) leads to the formation of columnar dendritic microstructures [6,33]. The columnar cells within each grain have been reported for numerous materials processed via AM including Ti alloys [20,34,35].

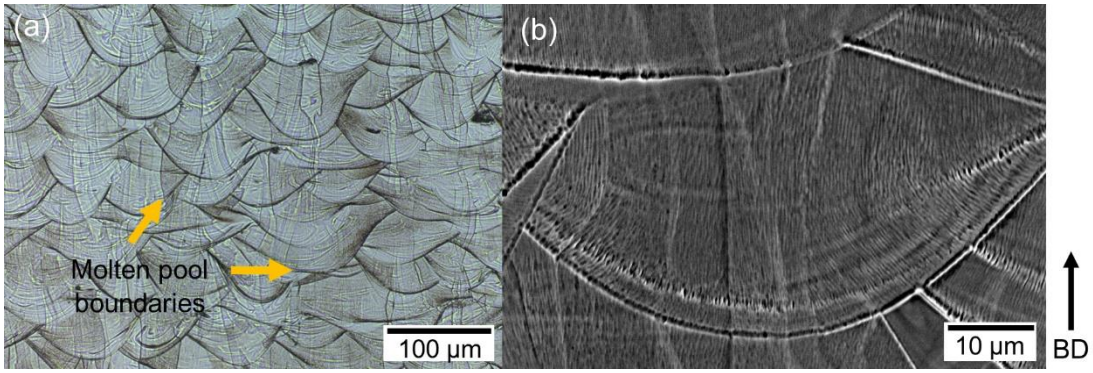

Figure 37 Images showing the microstructure after etching in AB condition at different magnifications (a) OM, (b) SEM

Texture was analyzed with EBSD in order to highlight the preferred crystallographic orientation. Figure 38 presents the EBSD orientation maps, the inverse pole figure (IPF) and pole figures, taken from the cross-sectional view of the AB sample. The black lines in the orientation maps denote the high angle grain boundaries (where misorientation > 15°). The microstructure observed is composed of large β-grains, mainly oriented along the building direction, with a preferred 〈001〉 alignment. The crystal growth occurs along the maximum temperature gradient, primarily formed parallel to the building direction, in the direction 〈001〉, which is known as the predominant-growth direction for BCC crystals [36,37] and was also found in PBF-LB of β-21S by Pellizari et al. [21]. Partial re-melting of the previous layers in PBF-LB process facilitates the grain growth from an existing grain, which acts as a the driving force for crystal growth in the same orientation [6]. It can be seen from Figure 38 the columnar grains propagated several hundreds of microns, larger than the molten pool depth of 70 µm, which confirms the epitaxial growth during PBF-LB.

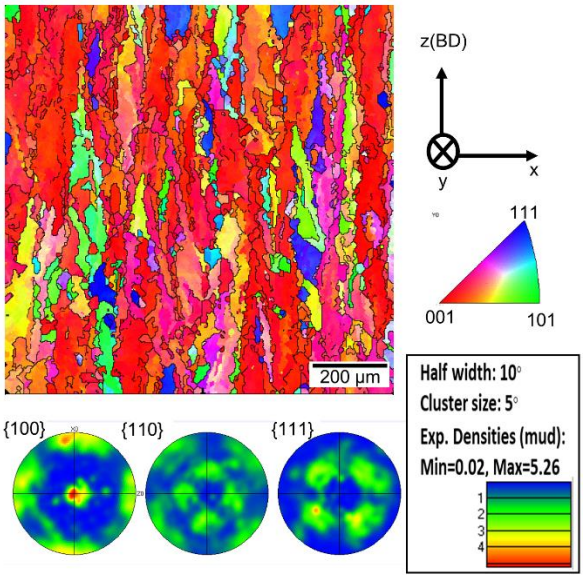

Figure 38 EBSD analysis of the AB sample

4.5.2 Microstructural characterization of STA

Figure **39** presents the XRD pattern of the STA sample. Peaks corresponding to α-phase (HCP, PDF 04-017-1339 [25]) and β-phase (BCC, PDF 04-020-9142 [25]) were identified. The α-phase is produced by the aging treatment, as discussed before.

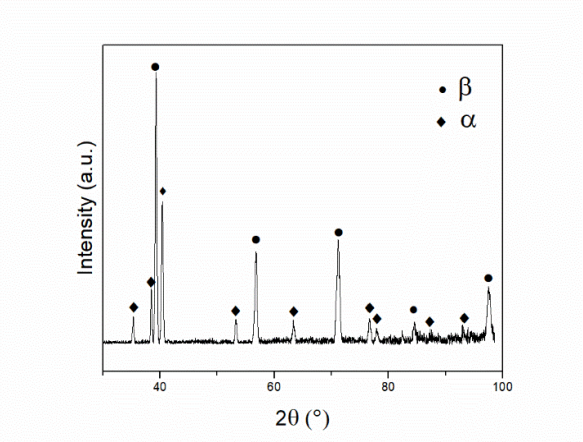

Figure 39 XRD pattern STA condition

Figure 40 presents SEM micrographs of a sample after STA. As expected, the melt pool boundaries observed in the AB condition are no longer present due to the thermal treatment applied to the

sample. The microstructure is composed of β-grains with α-phase at the grain boundaries (α_{GB}), α-plates within the grains and a zone free of precipitation (PFZ), indicated by arrows. The measured thickness of the α_{GB} was in the scale of 0.25 ± 0.1 μm. The α_{GB} interdistance was 5 ± 4 μm. The size of the plates was measured to be 1 ± 1 μm and 0.2 ± 1 μm, for length and width, respectively. The explanation for these morphologies is as follows.

During aging, precipitation of α-phase take place on precursors, and on defect sites, such as grain boundaries, dislocations, and point defects [10,13,4]. Grain boundaries are the preferential nucleation sites in diffusional transformations, the formation of α_{GB} occurs as the prior β-grain boundaries serves as nucleation sites of α precipitation [38,39]. This is due to the fact that defects lower the nucleation barrier for phase nucleation.

At the same time, α-phase will nucleate in the interior of the grains on defect sites, such as vacancies generated during the rapid solidification, and grow into plates. As previously mentioned Agarwal et al. [19] and Huang et al. [4] reported β-21S produced by non AM techniques with STA (810-845°C, 30 min-1h, AC; 538-540°C, 8h, AC) [4,19] resulted in β hexagonal grains with a stubby morphology of α-phase, while the microstructure obtained in this study with similar STA consisted of columnar β-grains with α-plates of larger size. The difference in the microstructure obtained can be explained by the differences on the manufacturing process. PBF-LB β-21S consisted on uniform β-grains with small percentage of α-phase, while other common manufacturing processes used to produce β-21S involve a deformation process that give rise to a nonuniform microstructure. β-21S microstructure before STA reported by Agarwal et al. and Huang et al. [4,19] consisted of β-grains with nonuniform recrystallization and larger percentage of second phase, causing more inhomogeneities that give rise to nucleation sites for α-phase during aging. More nucleation sites are beneficial for the precipitation of α-phase but limit its coarsening [40]. Therefore, a more uniform microstructure such as PBF-LB β-21S resulted in lower nucleation sites for the α-phase and extensive growth of α into plates. Another possible explanation can be found by considering that the α-phase is growing from a pre-existing β-phase. This means that incoherence effects, i.e. interfacial energy between the β-matrix and the growing α-phase place a role in the formation of a plate morphology. Further explanation on this is not pursued as it is beyond the scope of this work. In Agarwal et al. and Huang et al. studies [4,19] the volume fraction of α-phase was measured to be ~33 % while in this study is reported to be ~10%.

The PFZ are explained as follows. The α-phase start precipitating at grain boundaries during aging, which are preferential nucleation sites, removing solute from the adjacent matrix causing a precipitation depletion zone when aging [4]. A zone free of α-phase has also been reported before in the literature for β-21S in STA [10,4,19]. Figure 41 (a) presents high magnification BSE-Comp micrograph of the α-phase in the STA alloy before etching. EDS line scan presented in Figure 41 (c) shows that the α-phase is enriched in Al and Ti and depleted in Mo and Nb that are β-phase stabilizers [10].

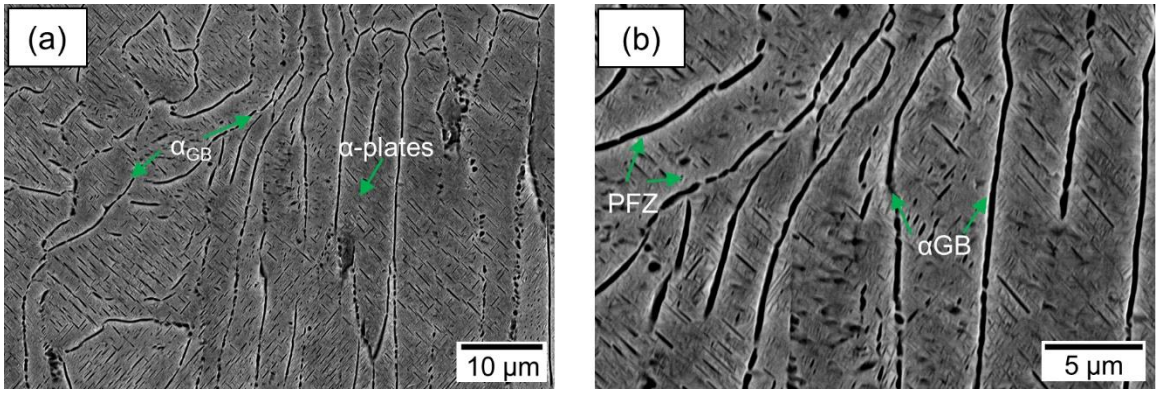

Figure 40 SEM micrographs showing the microstructure after etching of samples STA at different magnifications

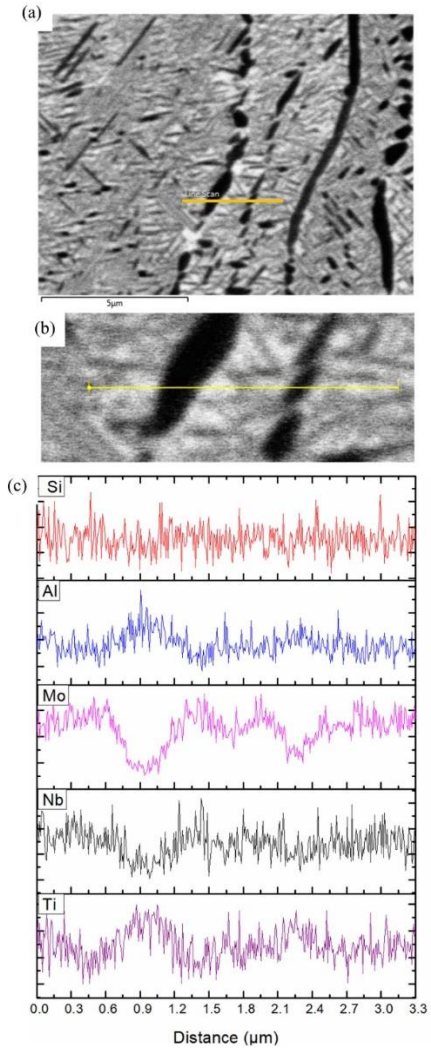

Figure 41 EDS line scan of the STA alloy

4.5.3 Mechanical properties

4.5.3.1 Hardness

β-21S is normally supplied in β ST condition [26] and used in aged condition. The microhardness obtained in the AB condition was 278 ± 5 HV, similar to the reported value of 274 HV for supplied β-21S ST at 843°C and AC (no aging) [41].

Our PBF-LB β-21S STA exhibited a value of 380 ± 13 HV. Similar to the reported hardness value for wrought β-21S STA (871 °C, 30min, AC; 538 °C, 8h, AC) of 400 HV [42]. As expected, the STA resulted in an increase of microhardness. This is due to the precipitation of the α-phase during

the heat treatment, the amount of α/β-phase interfaces increases. Phase interfaces can hinder the dislocations movement, causing the microhardness to increase [43].

4.5.3.2 Tensile properties AB RT

Figure 42 presents the PBF-LB β-21S YS and UTS as function of elongation in both AB and STA conditions. The Figure also includes some typical values of wrought β-21S ST and STA [18]. The results demonstrate that the PBF-LB β-21S has comparable mechanical properties to the wrought β-21S commonly used in the industry, with higher percentage of ductility attributed to the higher percentage of β-phase [44] presented in PBF-LB β-21S compared with wrought β-21S.

In order to further analyze these results, fracture surface was observed. Figure 43 presents the tensile fracture surface observed by SEM for the sample in the AB condition tested at RT. The specimen fractured in a ductile manner, as shown in Figure 43, dimples prevailed in the fracture surface. Dimples appear with the coalescence of voids formed during plastic deformation, in accordance with the high ductility presented on the AB sample. The observed dimple size of the AB sample was 10 ± 5 μm, that can be associated with the β-grain width.

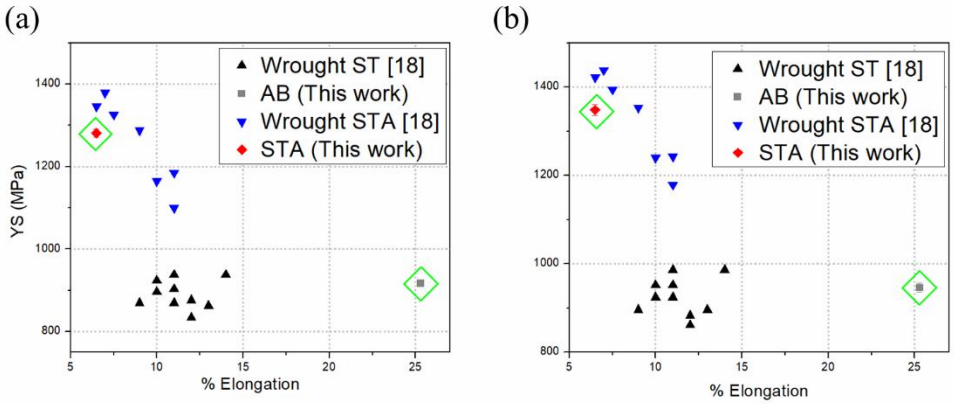

Figure 42 (a) YS, (b) UTS as a function of elongation at RT. Grey cube and red diamond denoted with green lines represent the values of β-21S in the present study: AB, and STA, respectively. Black triangles pointing up, and blue triangles pointing down represent wrought samples in: ST, and STA, respectively

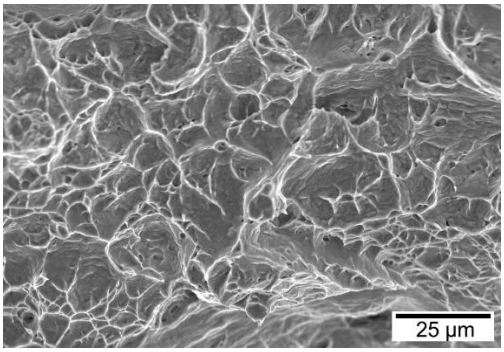

Figure 43 SEM micrograph of fracture surface. AB condition

4.5.3.3 Mechanical properties STA, RT

From Figure 42, it can be noted that PBF-LB β-21S STA provides competitive results of YS, UTS and elongation compared to wrought samples. In Figure 42, it can also be noted that STA of PBF-LB β-21S resulted in an increase of YS, and UTS, with a reduction of ductility. These changes are related to the precipitation of the α-phase. The α-precipitates act as barriers to dislocation slips [43,45,46]. Thus, give rise to the strengthening of the alloy while decrease ductility, since the α-plates prevent motion of dislocations [47], as they are small and distributed dispersedly within the β matrix, they act as barriers to dislocation slips. Figure 44 presents the tensile fracture surface of the PBF-LB β-21S STA tested at RT. The fracture surface primarily featured quasi-cleavage facets, as well as intergranular features. These observations are consistent with the lower ductility presented in the STA, respect to the AB condition. This result can be related to the microstructure. α_{GB} contributed to the intergranular fracture [48], and at the same time, to reduce the ductility. The α_{GB} provides long soft zones that deform preferentially during deformation causing high stress concentrations and resulted in separation of grains [10,49,50]. At the same time, it is suggested by Qin et al. [49], that the transgranular shearing occurs in the region between the tips of two cracks when the crack reaches a critical dimension in β-titanium alloys. On the other hand, dimples of size 1.5 ± 1 µm were also observed, which can be associated to the presence of α-plates, since the interfacial cohesion strength between the α and β-phases can lead to the formation of void at the α/β interface.

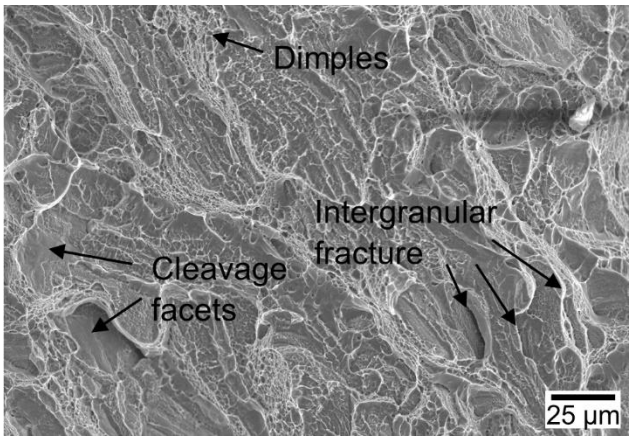

Figure 44 SEM micrographs of fracture surface at different magnification. STA condition

4.5.3.4 Mechanical properties at 450°C

Non-aged β-alloys are not commercially used at high temperatures as the β-phase prior to aging is metastable and, when exposed to elevated temperatures, is prone to phase transformation and stabilization, altering the properties [19,51]. Thus, only the sample in STA condition was tested at 450 °C. Figure 45 shows the YS and UTS along with its elongation values for the STA samples from the present work, with comparison to values of the wrought β-21S STA tested at 450°C [18]. The results obtained are similar to reported typical values as can be seen in the graphs. Compared to PBF-LB β-21S STA tested at RT, testing at 450 °C resulted in reduced YS and UTS, while the percentage of elongation slightly increased. Increasing temperature is associated with thermally activated processes, such as decrease in dislocation density, that result in reduction of strength at elevated temperatures in Ti-alloys [52]. Figure 46 presents SEM micrographs of fracture surface at 450 °C for the STA condition. As can be seen, dimples prevailed along the surface. The dimple size is 2 ± 1 μm, slightly larger than in the STA RT test. Similar to the RT test, void formation can be formed at the α/β interface. It is suggested that void growth occurred with increasing test temperature, while the difference in strength between the β-grain and α_{GB} decreased [53], diminishing the effect of α_{GB} on intergranular fracture. This behavior agrees with the small increase in ductility and reduction in strength presented at increased testing temperature.

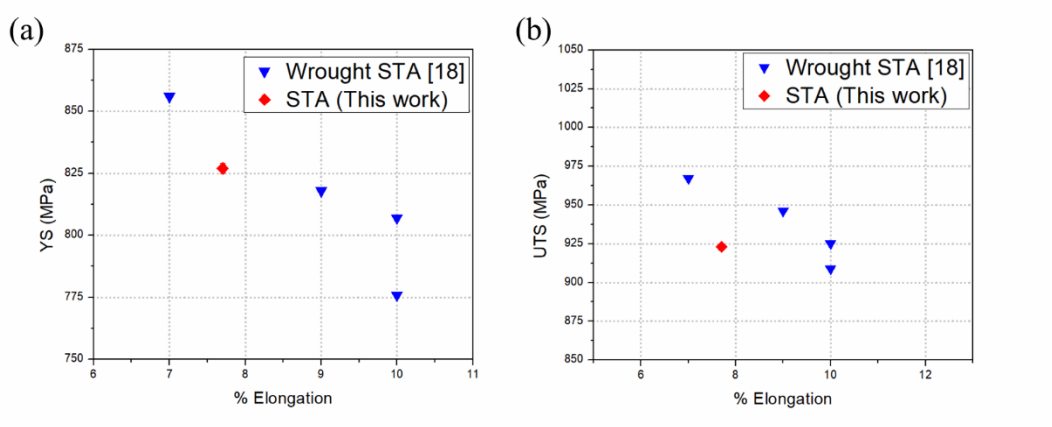

Figure 45 (a) YS, (b) UTS as a function of elongation at 450 °C. Red diamonds represent the values of β-21S STA in the present study. Triangles represent wrought samples in STA condition

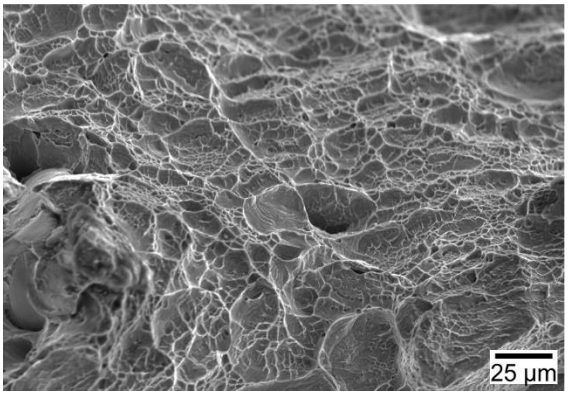

Figure 46 SEM micrographs of fracture surface at 450°C, STA condition

4.6 Conclusions

β-21S alloy samples were produced by PBF-LB. No second phase was detected by XRD and OM, and only β-phase was observed in the as-built condition. Further examination under EBSD demonstrated a small percentage of a α-phase. The crystallographic texture of the β-phase was analyzed. The preferential {001}〈100〉 crystallographic orientation and the formation of elongated grains along the building direction were observed. The samples presented a microhardness of 278 ± 5 HV, YS of 917 ± 1 MPa, UTS of 946 ± 19 MPa, and high ductility (25.3 ± 3 %), which are comparable properties to β-21S produced by non-AM techniques with posterior ST. The β solution treating of the sample at 850ºC for 30 minutes and subsequent aging at 538 ºC

for 8 h, both with AC, caused an increase in microhardness to 380 ± 13 HV, YS to 1281 ± 6 MPa, and UTS to 1348 ± 4 MPa and reduced ductility to 6.5 ± 1 % due to the precipitation of α-phase. At elevated temperature (450 ^{o}C), the heat-treated alloy presented a YS of 827 MPa, UTS of 923 MPa and a ductility of 7.7 %.

This work has shown that metastable β-21S Ti alloy is a promising candidate material for additive manufacturing processes with properties behaving according to the traditional heat treatment schedule.

Future research on PBF-LB might extend the explanations of α-precipitation on the AB condition. In addition, studies considering different aging time might prove an important area for future research to better understand the α-precipitation after STA.

References for Chapter 4

1. Dirk Herzog VS, Eric Wycisk, Claus Emmelmann (2016) Additive manufacturing of metals. Acta Materialia 117:371 - 392. doi:https://doi.org/10.1016/j.actamat.2016.07.019
2. O. Sanchez-Mata JAM-L, X. Wang, S.E. Atabay, M. Attarian Shandiz, M. Brochu (2020) Microstructure and mechanical properties at room and elevated temperature of crack-free Hastelloy X fabricated by laser powder bed fusion. Materials Science and Engineering: A 780:139177. doi:https://doi.org/10.1016/j.msea.2020.139177
3. Wang X, Muñiz-Lerma JA, Sanchez-Mata O, Atabay SE, Attarian Shandiz M, Brochu M (2020) Single-crystalline-like stainless steel 316L with different geometries fabricated by laser powder bed fusion. Progress in Additive Manufacturing 5 (1):41-49. doi:https://doi.org/10.1007/s40964-020-00123-9
4. Huang X, Cuddy J, Goel N, Richards NL (1994) Effect of heat treatment on the microstructure of a metastable β-titanium alloy. Journal of Materials Engineering and Performance 3 (4):560-566. doi:https://doi.org/10.1007/BF02645322
5. Kai Dietrich JD, Sophie Dubiez-Le Goff, Dominik Bauer, Pierre Forêt, Gerd Witt (2020) The influence of oxygen on the chemical composition and mechanical properties of Ti-6Al-4V during laser powder bed fusion (L-PBF). Additive Manufacturing 32:100980. doi:https://doi.org/10.1016/j.addma.2019.100980
6. Sıla Ece Atabay OS-M, Jose Alberto Muñiz-Lerma, Raynald Gauvin, Mathieu Brochu (2020) Microstructure and mechanical properties of rene 41 alloy manufactured by laser powder bed fusion. Materials Science and Engineering: A 773:138849. doi:https://doi.org/10.1016/j.msea.2019.138849
7. B. Pazhanivel PS, G. Sozhan (2020) Ultra-fine bimodal (α + β) microstructure induced mechanical strength and corrosion resistance of Ti-6Al-4V alloy produced via laser powder bed fusion process. Optics & Laser Technology 125:106017. doi:https://doi.org/10.1016/j.optlastec.2019.106017
8. Chaudhuri K, Perepezko JH (1994) Microstructural study of the titanium alloy Ti-15Mo-2.7Nb-3Al-0.2Si (TIMETAL 21S). Metallurgical and Materials Transactions A 25 (6):1109-1118. doi:https://doi.org/10.1007/BF02652286
9. Bania PJ (1991) Next Generation Titanium Alloys for Elevated Temperature Service. ISIJ International 31 (8):840-847. doi:https://doi.org/10.2355/isijinternational.31.840
10. Ian Polmear DS, Jian-Feng Nie, Ma Qian (2017) 7 - Titanium Alloys. In., "Fifth Edition" edn., pp 369 - 460. doi:https://doi.org/10.1016/B978-0-08-099431-4.00007-5
11. S.A. Mantri DC, T. Alam, G.B. Viswanathan, J.M. Sosa, H.L. Fraser, R. Banerjee (2018) Tuning the scale of α precipitates in β-titanium alloys for achieving high strength. Scripta Materialia 154:139 - 144. doi:https://doi.org/10.1016/j.scriptamat.2018.05.040
12. Chennakesava Sai Pitchi AP, Ganesh Sana, Suresh Kumar Reddy Narala (2020) A review on alloy composition and synthesis of β-Titanium alloys for biomedical applications. Materials Today: Proceedings 26:3297-3304. doi:https://doi.org/10.1016/j.matpr.2020.02.468
13. S Malinov WS, P Markovsky (2003) Experimental study and computer modelling of the β⇒α+β phase transformation in β21s alloy at isothermal conditions. Journal of Alloys and Compounds 348 (1):110 - 118. doi:https://doi.org/10.1016/S0925-8388(02)00804-6
14. O.M. Ivasishin PEM, Yu.V. Matviychuk, S.L. Semiatin, C.H. Ward, S. Fox (2008) A comparative study of the mechanical properties of high-strength β-titanium alloys. Journal of Alloys and Compounds 457 (1):296 - 309. doi:https://doi.org/10.1016/j.jallcom.2007.03.070

15. S.A. Mantri DC, A. Behera, M. Hendrickson, T. Alam, R. Banerjee (2019) Role of isothermal omega phase precipitation on the mechanical behavior of a Ti-Mo-Al-Nb alloy. Materials Science and Engineering: A 767:138397. doi:https://doi.org/10.1016/j.msea.2019.138397
16. Froes FH (2001) Titanium: Alloying. In: K.H. Jürgen Buschow RWC, Merton C. Flemings, Bernhard Ilschner, Edward J. Kramer, Subhash Mahajan, Patrick Veyssière (ed) Encyclopedia of Materials: Science and Technology. Elsevier, pp 9361 - 9364. doi:https://doi.org/10.1016/B0-08-043152-6/01690-9
17. Chuan Wu MZ (2019) Microstructural evolution, mechanical properties and fracture toughness of near β titanium alloy during different solution plus aging heat treatments. Journal of Alloys and Compounds 805:1144 - 1160. doi:https://doi.org/10.1016/j.jallcom.2019.07.134
18. Boyer R, Welsch G, Collings EW (1993) 54. TIMETAL® 21S. Materials Properties Handbook - Titanium Alloys. ASM International, United States of America
19. Agarwal N, Bhattacharjee A, Ghosal P, Nandy TK, Sagar PK (2008) Heat treatment, microstructure and mechanical properties of a metastable β titanium alloy timetal® 21s. Transactions of the Indian Institute of Metals 61 (5):419-425. doi:https://doi.org/10.1007/s12666-008-0074-6
20. Kreitcberg A, Brailovski V, Sheremetyev V, Prokoshkin S (2017) Effect of Laser Powder Bed Fusion Parameters on the Microstructure and Texture Development in Superelastic Ti–18Zr–14Nb Alloy. Shape Memory and Superelasticity 3 (4):361-372. doi:https://doi.org/10.1007/s40830-017-0125-0
21. Pellizzari M, Alireza Jam, Matilde Tschon, Milena Fini, Carlo Lora, and Matteo Benedetti (2020) A 3D-Printed Ultra-Low Young's Modulus β-Ti Alloy for Biomedical Applications. Materials 13:2792
22. G. Yablokova MS, J. Van Humbeeck, J.-P. Kruth, J. Schrooten, R. Cloots, F. Boschini, G. Lumay, J. Luyten (2015) Rheological behavior of β-Ti and NiTi powders produced by atomization for SLM production of open porous orthopedic implants. Powder Technology 283:199 - 209. doi:https://doi.org/10.1016/j.powtec.2015.05.015
23. Schneider CA, Rasband WS, Eliceiri KW (2012) NIH Image to ImageJ: 25 years of image analysis. Nature Methods 9 (7):671-675. doi:https://doi.org/10.1038/nmeth.2089
24. William D. Brewer RKB, Terryl A. Wallace (1998) Titanium alloys and processing for high speed aircraft. Materials Science and Engineering: A 243 (1):299 - 304. doi:https://doi.org/10.1016/S0921-5093(97)00818-6
25. Blanton SG-RT (2019) The Powder Diffraction File: A quality materials characterization database. Powder Diffraction 34 (4):352-360. doi:https://doi.org/10.1017/S0885715619000812
26. Kolli RP, Devaraj A (2018) A Review of Metastable Beta Titanium Alloys. Metals 8:506. doi:https://doi.org/10.3390/met8070506
27. Ivasishin OM, Markovsky PE, Matviychuk YV, Semiatin SL (2003) Precipitation and recrystallization behavior of beta titanium alloys during continuous heat treatment. Metallurgical and Materials Transactions A 34 (1):147-158. doi:https://doi.org/10.1007/s11661-003-0216-8
28. J-O Andersson TH, Lars Höglund, Pingfang Shi, Bo Sundman (2002) Thermo-Calc & DICTRA, computational tools for materials science. Calphad 26 (2):273 - 312. doi:https://doi.org/10.1016/S0364-5916(02)00037-8
29. Thampy V, Fong AY, Calta NP, Wang J, Martin AA, Depond PJ, Kiss AM, Guss G, Xing Q, Ott RT, van Buuren A, Toney MF, Weker JN, Kramer MJ, Matthews MJ, Tassone CJ, Stone KH

(2020) Subsurface Cooling Rates and Microstructural Response during Laser Based Metal Additive Manufacturing. Scientific Reports 10 (1):1981. doi:10.1038/s41598-020-58598-z
30. Zhao C, Fezzaa K, Cunningham RW, Wen H, De Carlo F, Chen L, Rollett AD, Sun T (2017) Real-time monitoring of laser powder bed fusion process using high-speed X-ray imaging and diffraction. Scientific Reports 7 (1):3602. doi:https://doi.org/10.1038/s41598-017-03761-2
31. M Gäumann SH, F Cléton, J.-D Wagnière, W Kurz (1999) Epitaxial laser metal forming: analysis of microstructure formation. Materials Science and Engineering: A 271 (1):232 - 241. doi:https://doi.org/10.1016/S0921-5093(99)00202-6
32. G.P. Dinda AKD, J. Mazumder (2009) Laser aided direct metal deposition of Inconel 625 superalloy: Microstructural evolution and thermal stability. Materials Science and Engineering: A 509 (1):98 - 104. doi:https://doi.org/10.1016/j.msea.2009.01.009
33. B. Vrancken LT, J.-P. Kruth, J. Van Humbeeck (2014) Microstructure and mechanical properties of a novel β titanium metallic composite by selective laser melting. Acta Materialia 68:150 - 158. doi:https://doi.org/10.1016/j.actamat.2014.01.018
34. Wei Chen CC, Xuhui Zi, Xiaofan Cheng, Xiaoyong Zhang, Yong Cheng Lin, Kechao Zhou (2018) Controlling the microstructure and mechanical properties of a metastable β titanium alloy by selective laser melting. Materials Science and Engineering: A 726:240 - 250. doi:https://doi.org/10.1016/j.msea.2018.04.087
35. H. Schwab FP, U. Kühn, J. Eckert (2016) Microstructure and mechanical properties of the near-beta titanium alloy Ti-5553 processed by selective laser melting. Materials & Design 105:75 - 80. doi:https://doi.org/10.1016/j.matdes.2016.04.103
36. Takeshi Nagase TH, Mitsuharu Todai, Shi-Hai Sun, Takayoshi Nakano (2019) Additive manufacturing of dense components in beta-titanium alloys with crystallographic texture from a mixture of pure metallic element powders. Materials & Design 173:107771. doi:https://doi.org/10.1016/j.matdes.2019.107771
37. A.T. Sidambe YT, P.B. Prangnell, P. Fox (2019) Effect of processing parameters on the densification, microstructure and crystallographic texture during the laser powder bed fusion of pure tungsten. International Journal of Refractory Metals and Hard Materials 78:254 - 263. doi:https://doi.org/10.1016/j.ijrmhm.2018.10.004
38. Yuyong Chen ZD, Shulong Xiao, Lijuan Xu, Jing Tian (2014) Effect of aging heat treatment on microstructure and tensile properties of a new β high strength titanium alloy. Journal of Alloys and Compounds 586:588 - 592. doi:https://doi.org/10.1016/j.jallcom.2013.10.096
39. Furuhara T, Takagi S, Watanabe H, Maki T (1996) Crystallography of grain boundary α precipitates in a β titanium alloy. Metallurgical and Materials Transactions A 27 (6):1635-1646. doi:https://doi.org/10.1007/BF02649821
40. T.W. Xu JSL, S.S. Zhang, F.S. Zhang, X.H. Liu (2016) Cold deformation behavior of the Ti-15Mo-3Al-2.7Nb-0.2Si alloy and its effect on α precipitation and tensile properties in aging treatment. Journal of Alloys and Compounds 682:404 - 411. doi:https://doi.org/10.1016/j.jallcom.2016.04.293
41. Wilson T (2017) β21S titanium alloy heat treatment development and improvement. Bachelor of Engineering, University of Queensland
42. George A. Young JRS (1993) Effects of hydrogen on the mechanical properties of a TiMoNbAl alloy. Scripta Metallurgica et Materialia 28 (4):507 - 512. doi:https://doi.org/10.1016/0956-716X(93)90091-6

43. Bei He JL, Xu Cheng, Hua-Ming Wang (2017) Brittle fracture behavior of a laser additive manufactured near-β titanium alloy after low temperature aging. Materials Science and Engineering: A 699:229 - 238. doi:https://doi.org/10.1016/j.msea.2017.05.050
44. Swee Leong Sing WYY, Florencia Edith Wiria (2016) Selective laser melting of titanium alloy with 50 wt% tantalum: Microstructure and mechanical properties. Journal of Alloys and Compounds 660:461 - 470. doi:https://doi.org/10.1016/j.jallcom.2015.11.141
45. Wenguang Zhu QS, Changsheng Tan, Pei Li, Lin Xiao, Jun Sun (2020) Tensile brittleness and ductility improvement in a novel metastable β titanium alloy with lamella structure. Journal of Alloys and Compounds 827:154311. doi:https://doi.org/10.1016/j.jallcom.2020.154311
46. Dipankar Banerjee JCW (2013) Perspectives on Titanium Science and Technology. Acta Materialia 61 (3):844 - 879. doi:https://doi.org/10.1016/j.actamat.2012.10.043
47. Jiangkun Fan JL, Hongchao Kou, Ke Hua, Bin Tang, Yudong Zhang (2016) Microstructure and mechanical property correlation and property optimization of a near β titanium alloy Ti-7333. Journal of Alloys and Compounds 682:517 - 524. doi:https://doi.org/10.1016/j.jallcom.2016.04.303
48. Chesnutt JC, Froes FH (1977) Effect of α-phase morphology and distribution on the tensile ductility of a metastable beta titanium alloy. Metall Trans, A 8 (6):1013-1017
49. Dongyang Qin YL, Qian Liu, Li Zheng, Lian Zhou (2013) Transgranular shearing introduced brittlement of Ti–5Al–5V–5Mo–3Cr alloy with full lamellar structure at room temperature. Materials Science and Engineering: A 572:19 - 24. doi:https://doi.org/10.1016/j.msea.2013.02.029
50. Dongyang Qin YL, Qian Liu, Lian Zhou (2013) Effects of Si addition on mechanical properties of Ti–5Al–5V–5Mo–3Cr alloy. Materials Science and Engineering: A 561:460 - 467. doi:https://doi.org/10.1016/j.msea.2012.10.063
51. Mantri SA, Choudhuri D, Behera A, Cotton JD, Kumar N, Banerjee R (2015) Influence of Fine-Scale Alpha Precipitation on the Mechanical Properties of the Beta Titanium Alloy Beta-21S. Metallurgical and Materials Transactions A 46 (7):2803-2808. doi:https://doi.org/10.1007/s11661-015-2944-y
52. R.C. Picu AM (2002) Mechanical behavior of Ti–6Al–4V at high and moderate temperatures—Part II: constitutive modeling. Materials Science and Engineering: A 326 (2):306 - 316. doi:https://doi.org/10.1016/S0921-5093(01)01508-8
53. Youngmoo Kim Y-BS, Sung Ho Lee (2015) Microstructure and intermediate-temperature mechanical properties of powder metallurgy Ti–6Al–4V alloy prepared by the prealloyed approach. Journal of Alloys and Compounds 637:234 - 241. doi:https://doi.org/10.1016/j.jallcom.2015.03.019

Chapter 6 – Conclusion and summary

The manufacturability of β-21S produced by LPBF, as well as the effect of heat treatment was investigated in the present thesis, to understand the relationship between the microstructure and the mechanical properties. The present thesis has made the following contributions to the field:

- The manufacturability of β-21S alloy produced by LPBF was evaluated. Dense samples were obtained and, the mechanical properties were found to behave according to the traditional heat treatment schedule.
- The microstructure obtained after LPBF consisted of β-phase and a small percentage of a α-phase.
- The crystallographic texture of the β-phase was found to have a preferential {001}〈100〉 crystallographic orientation and the formation of elongated grains along the building direction were observed.
- The samples presented a microhardness of 278 ± 5 HV, YS of 917 ± 1 MPa, UTS of 946 ± 19 MPa, and high ductility (25.3 ± 3 %), which are comparable properties to β-21S produced by non-AM techniques with posterior ST.
- The response of the LPBF parts to conventional heat treatment was evaluating, targeting application in the aerospace industry. The β solution treating of the sample at 850 °C for 30 minutes and subsequent aging at 538 °C for 8 h, both with AC, caused an increase in microhardness to 380 ± 13 HV, YS to 1281 ± 6 MPa, and UTS to 1348 ± 4 MPa and reduced ductility to 6.5 ± 1 % due to the precipitation of α-phase. These properties were found to be similar to β-21S fabricated by non-AM techniques.
- This thesis presents, for the first time, the mechanical properties at high temperature for the LPBF β-21S.
- At elevated temperature (450 °C), the heat-treated alloy presented a YS of 827 MPa, UTS of 923 MPa and a ductility of 7.7 %.
- This thesis proves β-21S is an ideal candidate for LPBF, as the mechanical properties found to behave according to the selected heat-treatment. Different heat-treatments can be studied to further tailor the properties for different applications.

Chapter 7 – Master Reference list

The following references are associated to Chapters 1, 2 and 3.

1. Frazier WEJJoME, performance (2014) Metal additive manufacturing: a review. 23 (6):1917-1928
2. Gebhardt A (2011) Understanding additive manufacturing.
3. Calignano F (2018) Investigation of the accuracy and roughness in the laser powder bed fusion process. Virtual and Physical Prototyping 13 (2):97-104. doi:10.1080/17452759.2018.1426368
4. J.P. Oliveira ADL, J. Ma (2020) Processing parameters in laser powder bed fusion metal additive manufacturing. Materials & Design 193:108762. doi:https://doi.org/10.1016/j.matdes.2020.108762
5. Kurzynowski T, Pawlak A, Smolina I (2020) The potential of SLM technology for processing magnesium alloys in aerospace industry. Archives of Civil and Mechanical Engineering 20 (1):23. doi:10.1007/s43452-020-00033-1
6. Gibson I, Rosen D, Stucker B, Khorasani M (2014) Additive manufacturing technologies, vol 17. Springer,
7. Kumara C, Balachandramurthi AR, Goel S, Hanning F, Moverare J (2020) Toward a better understanding of phase transformations in additive manufacturing of Alloy 718. Materialia 13:100862. doi:https://doi.org/10.1016/j.mtla.2020.100862
8. Frazier WE (2014) Metal Additive Manufacturing: A Review. Journal of Materials Engineering and Performance 23 (6):1917-1928. doi:10.1007/s11665-014-0958-z
9. Zhao S, Li SJ, Hou WT, Hao YL, Yang R, Misra RDK (2016) The influence of cell morphology on the compressive fatigue behavior of Ti-6Al-4V meshes fabricated by electron beam melting. Journal of the mechanical behavior of biomedical materials 59:251-264. doi:10.1016/j.jmbbm.2016.01.034
10. Zhang XY, Fang G, Leeflang S, Böttger AJ, A. Zadpoor A, Zhou J (2018) Effect of subtransus heat treatment on the microstructure and mechanical properties of additively manufactured Ti-6Al-4V alloy. Journal of Alloys and Compounds 735:1562-1575. doi:10.1016/j.jallcom.2017.11.263
11. Muñiz-Lerma JA, Tian Y, Wang X, Gauvin R, Brochu M (2019) Microstructure evolution of Inconel 738 fabricated by pulsed laser powder bed fusion. Progress in Additive Manufacturing 4 (2):97-107. doi:10.1007/s40964-018-0062-2
12. G.P. Dinda AKD, J. Mazumder (2009) Laser aided direct metal deposition of Inconel 625 superalloy: Microstructural evolution and thermal stability. Materials Science and Engineering: A 509 (1):98 - 104. doi:https://doi.org/10.1016/j.msea.2009.01.009
13. Wang X, Muñiz-Lerma JA, Sanchez-Mata O, Atabay SE, Attarian Shandiz M, Brochu M (2020) Single-crystalline-like stainless steel 316L with different geometries fabricated by laser powder bed fusion. Progress in Additive Manufacturing 5 (1):41-49. doi:https://doi.org/10.1007/s40964-020-00123-9
14. Lewandowski JJ, Seifi M (2016) Metal Additive Manufacturing: A Review of Mechanical Properties. 46 (1):151-186. doi:10.1146/annurev-matsci-070115-032024
15. Shi R, Khairallah S, Heo TW, Rolchigo M, McKeown JT, Matthews MJ (2019) Integrated Simulation Framework for Additively Manufactured Ti-6Al-4V: Melt Pool Dynamics, Microstructure, Solid-State Phase Transformation, and Microelastic Response. JOM 71 (10):3640-3655. doi:10.1007/s11837-019-03618-1

16. Cepeda-Jiménez CM, Potenza F, Magalini E, Luchin V, Molinari A, Pérez-Prado MT (2020) Effect of energy density on the microstructure and texture evolution of Ti-6Al-4V manufactured by laser powder bed fusion. Materials Characterization 163. doi:10.1016/j.matchar.2020.110238
17. Garcia-Colomo A, Wood D, Martina F, Williams S (2019) A comparison framework to support the selection of the best additive manufacturing process for specific aerospace applications. International Journal of Rapid Manufacturing 9. doi:10.1504/IJRAPIDM.2020.10019230
18. Kolli RP, Devaraj A (2018) A Review of Metastable Beta Titanium Alloys. Metals 8:506. doi:https://doi.org/10.3390/met8070506
19. Lütjering G, Williams JC (2007) Titanium. Springer Science & Business Media,
20. Bania PJ (1994) Beta titanium alloys and their role in the titanium industry. JOM 46 (7):16-19. doi:10.1007/BF03220742
21. S.A. Mantri DC, A. Behera, M. Hendrickson, T. Alam, R. Banerjee (2019) Role of isothermal omega phase precipitation on the mechanical behavior of a Ti-Mo-Al-Nb alloy. Materials Science and Engineering: A 767:138397. doi:https://doi.org/10.1016/j.msea.2019.138397
22. Maimaitiyili T, Mosur K, Kurzynowski T, Casati N, Swygenhoven HV (2020) Phase studies of additively manufactured near beta titanium alloy-Ti55511. Materials 13 (7). doi:10.3390/ma13071723
23. Cotton JD, Briggs RD, Boyer RR, Tamirisakandala S, Russo P, Shchetnikov N, Fanning JC (2015) State of the Art in Beta Titanium Alloys for Airframe Applications. JOM 67 (6):1281-1303. doi:10.1007/s11837-015-1442-4
24. Welsch G, Boyer R, Collings E (1993) Materials properties handbook: titanium alloys. ASM international,
25. Dipankar Banerjee JCW (2013) Perspectives on Titanium Science and Technology. Acta Materialia 61 (3):844 - 879. doi:https://doi.org/10.1016/j.actamat.2012.10.043
26. Agarwal N, Bhattacharjee A, Ghosal P, Nandy TK, Sagar PK (2008) Heat treatment, microstructure and mechanical properties of a metastable β titanium alloy timetal® 21s. Transactions of the Indian Institute of Metals 61 (5):419-425. doi:https://doi.org/10.1007/s12666-008-0074-6
27. Mantri SA, Choudhuri D, Behera A, Cotton JD, Kumar N, Banerjee R (2015) Influence of Fine-Scale Alpha Precipitation on the Mechanical Properties of the Beta Titanium Alloy Beta-21S. Metallurgical and Materials Transactions A 46 (7):2803-2808. doi:https://doi.org/10.1007/s11661-015-2944-y
28. Chaudhuri K, Perepezko JH (1994) Microstructural study of the titanium alloy Ti-15Mo-2.7Nb-3Al-0.2Si (TIMETAL 21S). Metallurgical and Materials Transactions A 25 (6):1109-1118. doi:https://doi.org/10.1007/BF02652286
29. O.M. Ivasishin PEM, Yu.V. Matviychuk, S.L. Semiatin, C.H. Ward, S. Fox (2008) A comparative study of the mechanical properties of high-strength β-titanium alloys. Journal of Alloys and Compounds 457 (1):296 - 309. doi:https://doi.org/10.1016/j.jallcom.2007.03.070
30. G. Lütjering JA, C. Sauer, T. Krull (2007) The influence of soft, precipitate-free zones at grain boundaries in Ti and Al alloys on their fatigue and fracture behavior. Materials Science and Engineering: A 468-470:201 - 209. doi:https://doi.org/10.1016/j.msea.2006.07.168
31. Ji X, Ge P, Xiang S, Tan Y (2021) Effects of Double-Ageing Heat Treatments on the Microstructure and Mechanical Behaviour of a Ti-3.5Al-5Mo-4V Alloy. 14 (1):209

32. Boyer R, Welsch G, Collings EW (1993) 54. TIMETAL® 21S. Materials Properties Handbook - Titanium Alloys. ASM International, United States of America
33. Agarwal N, Bhattacharjee A, Ghosal P, Nandy T, Sagar PJTotIIoM (2008) Heat treatment, microstructure and mechanical properties of a metastable β titanium alloy timetal® 21s. 61 (5):419-425
34. T.W. Xu JSL, S.S. Zhang, F.S. Zhang, X.H. Liu (2016) Cold deformation behavior of the Ti-15Mo-3Al-2.7Nb-0.2Si alloy and its effect on α precipitation and tensile properties in aging treatment. Journal of Alloys and Compounds 682:404 - 411. doi:https://doi.org/10.1016/j.jallcom.2016.04.293
35. Xu TW, Kou HC, Li JS, Zhang FS, Feng Y (2015) Effect of Phase Transformation Conditions on the Microstructure and Tensile Properties of Ti-3Al-15Mo-3Nb-0.2Si Alloy. Journal of Materials Engineering and Performance 24 (8):3018-3025. doi:10.1007/s11665-015-1583-1
36. Huang X, Cuddy J, Goel N, Richards NL (1994) Effect of heat treatment on the microstructure of a metastable β-titanium alloy. Journal of Materials Engineering and Performance 3 (4):560-566. doi:https://doi.org/10.1007/BF02645322
37. Bermingham MJ, Kent D, Pace B, Cairney JM, Dargusch MS (2020) High strength heat-treatable β-titanium alloy for additive manufacturing. Materials Science and Engineering A 791. doi:10.1016/j.msea.2020.139646
38. Deng H, Qiu W, Cao S, Chen L, Hu Z, Wei Y, Xia Z, Zhou L, Cui X, Tang J (2021) Heat-treatment induced microstructural evolution and enhanced mechanical property of selective laser melted near β Ti-5Al-5Mo-5 V-3Cr-1Zr alloy. Journal of Alloys and Compounds 858. doi:10.1016/j.jallcom.2020.158351
39. da Costa FH, Pinhão R, dos Anjos S, Caram R, Fogagnolo JB (2020) Stiffness and hardness gradients obtained by laser surface melting of an aged β-Ti alloy. Materials Letters 260. doi:10.1016/j.matlet.2019.126901
40. Polozov I, Kantyukov A, Goncharov I, Razumov N, Silin A, Popovich V, Zhu JN, Popovich A (2020) Additive manufacturing of Ti-48Al-2Cr-2Nb alloy using gas atomized and mechanically alloyed plasma spheroidized powders. Materials 13 (18). doi:10.3390/ma13183952
41. Nakano T, Ishimoto T, Matsugaki A, Hagihara K, Koizumi Y, Ozasa RJMWC (2020) Control of crystallographic orientation by metal additive manufacturing process of β-type Ti alloys based on the bone tissue anisotropy. 321:05002
42. Pham M-S, Dovgyy B, Hooper PA, Gourlay CM, Piglione A (2020) The role of side-branching in microstructure development in laser powder-bed fusion. Nature Communications 11 (1):749. doi:10.1038/s41467-020-14453-3
43. Sames WJ, List FA, Pannala S, Dehoff RR, Babu SS (2016) The metallurgy and processing science of metal additive manufacturing. International Materials Reviews 61 (5):315-360. doi:10.1080/09506608.2015.1116649
44. Takeshi Nagase TH, Mitsuharu Todai, Shi-Hai Sun, Takayoshi Nakano (2019) Additive manufacturing of dense components in beta-titanium alloys with crystallographic texture from a mixture of pure metallic element powders. Materials & Design 173:107771. doi:https://doi.org/10.1016/j.matdes.2019.107771
45. Pellizzari M, Alireza Jam, Matilde Tschon, Milena Fini, Carlo Lora, and Matteo Benedetti (2020) A 3D-Printed Ultra-Low Young's Modulus β-Ti Alloy for Biomedical Applications. Materials 13:2792

46. Zafari A, Lui EW, Xia K (2020) Deformation-free geometric recrystallisation in a metastable β-Ti alloy produced by selective laser melting. Materials Research Letters 8 (3):117-122. doi:10.1080/21663831.2020.1713244
47. Fischer M, Joguet D, Robin G, Peltier L, Laheurte P (2016) In situ elaboration of a binary Ti-26Nb alloy by selective laser melting of elemental titanium and niobium mixed powders. Materials Science and Engineering C 62:852-859. doi:10.1016/j.msec.2016.02.033
48. Fischer M, Joguet D, Robin G, Peltier L, Laheurte P (2016) In situ elaboration of a binary Ti–26Nb alloy by selective laser melting of elemental titanium and niobium mixed powders. Materials Science and Engineering: C 62:852-859. doi:https://doi.org/10.1016/j.msec.2016.02.033
49. Duan R, Li S, Cai B, Zhu W, Ren F, Attallah MM (2021) A high strength and low modulus metastable β Ti-12Mo-6Zr-2Fe alloy fabricated by laser powder bed fusion in-situ alloying. Additive Manufacturing 37:101708. doi:https://doi.org/10.1016/j.addma.2020.101708
50. B. Vrancken LT, J.-P. Kruth, J. Van Humbeeck (2014) Microstructure and mechanical properties of a novel β titanium metallic composite by selective laser melting. Acta Materialia 68:150 - 158. doi:https://doi.org/10.1016/j.actamat.2014.01.018
51. Qiu C, Liu Q (2019) Multi-scale microstructural development and mechanical properties of a selectively laser melted beta titanium alloy. Additive Manufacturing 30. doi:10.1016/j.addma.2019.100893
52. G. Yablokova MS, J. Van Humbeeck, J.-P. Kruth, J. Schrooten, R. Cloots, F. Boschini, G. Lumay, J. Luyten (2015) Rheological behavior of β-Ti and NiTi powders produced by atomization for SLM production of open porous orthopedic implants. Powder Technology 283:199 - 209. doi:https://doi.org/10.1016/j.powtec.2015.05.015
53. Schneider CA, Rasband WS, Eliceiri KW (2012) NIH Image to ImageJ: 25 years of image analysis. Nature Methods 9 (7):671-675. doi:https://doi.org/10.1038/nmeth.2089
54. Britannica TEoE "Archimedes' principle.".